The Cryosphere Discussions

Simulating melt, runoff and refreezing on Nordenskiöldbreen, Svalbard, using a coupled snow and energy balance model

W. J. J. van Pelt[1], **J. Oerlemans**[1], **C. H. Reijmer**[1], **V. A. Pohjola**[2], **R. Pettersson**[2], **and J. H. van Angelen**[1]

[1]Institute for Marine and Atmospheric research, Utrecht University, Utrecht, The Netherlands
[2]Department of Earth Sciences, Uppsala University, Uppsala, Sweden

Correspondence to: W. J. J. van Pelt (w.j.j.vanpelt@uu.nl)

Title Page

Abstract	Introduction
Conclusions	References
Tables	Figures

Back | Close

Full Screen / Esc

Printer-friendly Version

Interactive Discussion

Melt, runoff and refreezing on Nordenskiöldbreen

W. J. J. van Pelt et al.

Abstract

A distributed energy balance model is coupled to a multi-layer snow model in order to study the mass balance evolution and the impact of refreezing on the mass budget of Nordenskiöldbreen, Svalbard. The model is forced with output of a regional climate model (RACMO) and meteorological data from Svalbard Airport. Extensive calibration and initialisation are performed to increase the model accuracy. For the period 1989–2010, we find a mean net mass balance of $-0.39\,\mathrm{m\,w.e.\,a^{-1}}$. Refreezing contributes on average $0.27\,\mathrm{m\,w.e.\,a^{-1}}$ to the mass budget and is most pronounced in the accumulation zone. The simulated mass balance, radiative fluxes and subsurface profiles are validated against observations and are generally in good agreement. Climate sensitivity experiments reveal a non-linear, seasonally dependent response of the mass balance, refreezing and runoff to changes in temperature and precipitation. Output of the climate sensitivity experiments is used in combination with temperature and precipitation time-series to extend mass balance time-series in the past and the future to obtain estimates for the period 1912–2085. It is shown that including seasonality in climate change, with less pronounced summer warming, has a major impact on future mass balance and ELA estimates. Due to compensating effects, the contribution of refreezing hardly changes in a future climate.

1 Introduction

The mass balance has been acknowledged as the critical link between glaciers and climate (Meier, 1965). Numerical models capable of simulating the surface mass balance have proven useful to analyse the temporal evolution and spatial distribution of the mass budget of ice masses in more detail than provided by observations only (Greuell, 1992; Hock, 1999). Additionally, mass balance models have been used as predictive tools to study the sensitivity of glaciers to climate change (Oerlemans et al., 1998; Braithwaite and Zhang, 1999; De Woul and Hock, 2005; Raper and Braithwaite, 2006;

Hock and Radic, 2007). Distributed mass balance models that solve the energy balance to compute melt have shown to be capable of simulating spatial melt patterns and their variability (Klok and Oerlemans, 2002; Hock and Holmgren, 2005).

Refreezing of percolating and stored water in snow and firn contributes significantly
5 to the mass balance of glaciers (Schytt, 1949; Koerner, 1970) and has a pronounced impact on the thermal structure (Greuell and Oerlemans, 1989; Paterson, 1994). Refreezing of percolating water is most pronounced in spring when low subsurface temperatures and the presence of a snow pack increase the potential for refreezing. During the melting season superimposed ice may form when percolating water accumulates a
10 slush layer on top of the cold impermeable ice layer and refreezes (Wadham and Nuttall, 2002; Obleitner and Lehning, 2004; Wright et al., 2005). After the melting season, water trapped in pore spaces is subject to refreezing when a cold wave penetrates into the snow/firn pack (Pfeffer et al., 1991). The latent heat release after refreezing raises subsurface temperatures and hence affects the heat flux from the surface
15 into the ice. Refreezing below the previous year's summer surface in the accumulation zone, referred to as internal accumulation, has received considerable attention, since this term is disregarded by traditional mass balance observations (Trabant and Mayo, 1985; Schneider and Jansson, 2004; Reijmer and Hock, 2008). Other studies show the significance of refreezing in the timing and rate of englacial water transport
20 (Pfeffer et al., 1991; Fountain, 1996; Jansson et al., 2003), which has substantial implications for basal dynamics (Zwally et al., 2002; Van de Wal et al., 2008; Schoof, 2010). Coupling of a distributed energy balance model to a snow model, which simulates the subsurface temperature, density and water evolution, is required to accurately simulate ice melt, refreezing and runoff, and study the relative impact of refreezing on the mass
25 budget of a glacier.

In this study, a distributed energy balance model, developed along the lines presented by Klok and Oerlemans (2002), is coupled to a multi-layer snow model, based on the SOMARS model (Simulation Of glacier surface Mass balance And Related Subsurface processes) described by Greuell and Konzelmann (1994), in order to

Melt, runoff and refreezing on Nordenskiöldbreen

W. J. J. van Pelt et al.

Title Page

Abstract | Introduction

Conclusions | References

Tables | Figures

◄◄ | ►►

◄ | ►

Back | Close

Full Screen / Esc

Printer-friendly Version

Interactive Discussion

simulate the spatial distribution and temporal evolution of the mass balance on Nordenskiöldbreen, Svalbard. The snow model computes vertical profiles of temperature, density and water content and accounts for subsurface water percolation, storage and runoff. Gridded meteorological input fields are constructed from output of the Regional Atmospheric Climate Model (RACMO) and weather station data from Svalbard Airport. Extensive calibration is performed to constrain values of model parameters, whereas comprehensive initialisation is done to attain subsurface profiles at the start of the simulation. The model is run over the period 1989–2010 and we present the evolution of the mass balance and energy balance and discuss this in connection with evolving subsurface properties. Sensitivity experiments are performed to investigate the sensitivity of the model output to the parameter setup, initial subsurface conditions and climate perturbations.

Mean surface temperatures at Svalbard Airport have risen by 0.22 °C per decade since 1912 and regional climate model projections for the 21st century predict a warming from 1961–1990 to 2071–2100 ranging from 3 °C in the southwest of Svalbard to 8 °C in the northeast (Førland et al., 2009). Temperature increase is expected to be less pronounced in summer than during the winter season. Regional differences and seasonal variations in climate change both have a significant impact on the sensitivity of the mass balance and should be accounted for in future mass balance projections. Output of the climate sensitivity experiments is used in combination with reconstructed and projected seasonal time-series of temperature and precipitation to extend the time-span of the mass balance time-series to the period 1912–2085.

2 Nordenskiöldbreen and grid

Nordenskiöldbreen is a large outlet glacier, situated in central Spitsbergen and connected to a large ice plateau, Lomonosovfonna. On its way down, ice flows around the two rock formations, Terrierfjellet and Ferrierfjellet, towards the Adolfbukta fjord. Until around the year 2000, the front of the glacier was known to be calving along its

full width. Following the recent retreat of the tongue, calving is now insignificant and the glacier can presently be classified as a grounded glacier. Calving may become significant again in the next few decades, as recent Ground Penetrating Radar (GPR) observations indicate bedrock heights below sea-level upstream of the current snout position.

A DEM of the glacier and its surroundings is derived from stereoscopic optical images, gathered in 2007 and provided by the SPIRIT project: SPOT 5 stereoscopic survey of Polar Ice: Reference Images and Topographies (Korona et al., 2009). Some processing of the DEM is done to remove erroneous spikes in the surface profile. The resulting gaps were filled using interpolation techniques. A contour plot of the surface topography is shown in Fig. 1.

The area of Nordenskiöldbreen, bounded by the black line in Fig. 1, is chosen to extend up to the estimated position of the ice divide, where horizontal ice flow is likely to be small. We therefore assume that the total mass budget of the selected grid is merely the sum of the surface mass balance and a negative mass flux by calving. The selected grid covers a total area of 193 km^2 and spans an altitudinal range of 0 to 1195 m above sea level (m a.s.l.). The highest point of the Lomonosovfonna ice cap is located at 1237 m a.s.l. Highest ice velocities are found along the main flow line between Terrierfjellet and De Geerfjellet, where mean surface velocities are typically in the range of 30–60 m per year (m a^{-1}) (Den Ouden et al., 2010). GPR observations indicate an ice thickness of up to more than 600 m along the flow line. The mean surface temperature and amount of precipitation measured at Svalbard Airport (28 m a.s.l.), situated ±55 km west of the glacier snout, over the period 1980–2010 are equal to −6.7 °C and 190 mm per year, respectively. Owing to the high latitude, seasonality in the temperature cycle is strong, with monthly mean extrema at Svalbard Airport ranging from −16.7 °C in February to +5.9 °C in July.

3 Data

In this study, data are used to: (1) construct meteorological input to force the surface energy balance model (Sect. 3.1), (2) calibrate poorly-constrained model parameters (Sect. 4.4), and (3) validate model results (Sect. 5.3). Continuous measurements with an Automatic Weather Station (AWS) on the glacier (Fig. 1), operated by the Institute for Marine and Atmospheric research Utrecht (IMAU) since March 2009, are employed for both calibration and validation purposes.

3.1 Meteorological input

Two sources of meteorological data are adopted to construct gridded spatial patterns of air temperature, humidity, precipitation, cloud cover and air pressure: (1) output of the Regional Atmospheric Climate Model (RACMO) and (2) meteorological data from Svalbard Airport (SA).

Cloud cover and precipitation estimates are constructed from meteorological time-series at Svalbard Airport. Cloud cover observations with a 6-hourly resolution are downscaled to the 3-h model resolution by interpolation, whereas 3-hourly values of the precipitation rate are constructed by homogeneous distribution of observed 12-hourly precipitation totals in time. On the grid cloud cover is assumed to be spatially invariant, whereas precipitation increases linearly with height at a calibrated rate of 370 mm per km (see Sect. 4.4). The mean observed precipitation rate at Svalbard Airport (27 m a.s.l.) over the period 1989–2010 of 191 mm is used to compute a mean altitude of 971 m a.s.l. above which precipitation is constant. The resulting yearly mean maximum precipitation of 540 mm per year over the period 1989–2010 is similar to the mean accumulation rate found by Pälli et al. (2002) on Nordenskiöldbreen for the period 1963–1999 using GPR measurements.

Gridded 3-hourly air temperature, pressure and specific humidity input is constructed from output of the Regional Atmospheric Climate Model (RACMO), as presented by Ettema et al. (2010). RACMO is forced at the boundaries with ERA-Interim

Melt, runoff and refreezing on Nordenskiöldbreen

W. J. J. van Pelt et al.

Title Page

Abstract	Introduction
Conclusions	References
Tables	Figures

◄◄   ►►

◄   ►

Back   Close

Full Screen / Esc

Printer-friendly Version

Interactive Discussion

reanalysis data, provided by the European Centre for Medium-Range Weather Forecasts (ECMWF), for the period 1989–2010. We use data from two RACMO grid points located within 2 km from the grid at altitudes of 461 and 957 m a.s.l. Every model time-step, altitudinal gradients of air temperature, specific humidity and potential temperature between the two RACMO grid points are used to linearly inter- and extrapolate these variables onto the grid. Air pressure is computed using gridded fields of air temperature and potential temperature. The sensible and latent heat flux formulations in the surface energy budget specifically require temperature and specific humidity input that is unaffected by the glacier's microclimate (Oerlemans and Grisogono, 2002). Therefore, RACMO humidity and temperature estimates at 32-m altitude above the glacier surface are used in the calculation of turbulent fluxes. Additionally, the 32-m temperatures are adopted in the computation of the incoming long wave radiation component. A comparison of 3-hourly gridded air temperatures at two altitudes and observed temperatures at ±4 m above the surface at the location of the AWS is shown in Fig. 2. The observations since 2009 unfortunately do not cover the melting season due to short-circuiting in the system. High correlations are found between the observed values and RACMO 32-m ($R = 0.96$) and 2-m ($R = 0.94$) temperatures, which demonstrates that temperature variations are well replicated in the RACMO dataset. The high correlations indicate the potential to use regional climate model data to construct input fields in regions where observations are scarce. Since we lack temperature observations unaffected by the glacier surface (typically at heights >10 m above the surface), no bias correction to the employed 32-m temperatures is applied. In the RACMO domain, Svalbard is located relatively close to the boundary, which leads to significant artifacts in cloud cover and precipitation estimates in this region. We therefore decided not to use RACMO data for those variables for further analysis.

3.2 Stake measurements and snow profiles

Since 2006, stake measurements are performed at multiple sites on the glacier (S1–11 in Fig. 1). Generally, stake readings have been done once a year in early spring and

Title Page

Abstract | Introduction

Conclusions | References

Tables | Figures

|◄ | ►|

◄ | ►

Back | Close

Full Screen / Esc

Printer-friendly Version

Interactive Discussion

provide estimates of surface height variations. Snow pits have been dug at several sites in 2008 and 2009 in order to measure vertical profiles of density and temperature. Furthermore, snow depth measurements at the stake locations are done to estimate the relative contribution of ice melt to the change in surface height. The mean observed

5 snow density of $372\,\mathrm{kg\,m^{-3}}$ is used in combination with the change in snow depth to convert the observed surface heights into mass balance estimates. Continuous surface height measurements with a Sonic Ranger in 2007 are used for model calibration, as described in Sect. 4.4.

In May 1997, a 121-m long ice core was drilled near the summit of the Lomonosov-

10 fonna (DS in Fig. 1). A 36-m deep vertical density profile was constructed and presented by Pohjola et al. (2002b). Borehole temperatures were measured down to the bottom of the ice core, and have been analysed by Van de Wal et al. (2002). The role of these vertical profiles in the derivation of initial subsurface conditions at the start of the simulation is discussed in Sect. 4.5.

15 4   Model setup

In this study, a distributed energy balance model is coupled to a snow model and applied to Nordenskiöldbreen. The two models are coupled in the sense that melt water production at the surface serves as input for the snow model, which simulates storage and refreezing of percolating water. Furthermore, the models are coupled through the

20 subsurface heat flux, which affects the surface energy budget and depends on vertical profiles of temperature and density.

The specific mass balance at a certain location on the glacier is defined as the accumulated exchange of mass per unit area over a period of time, often expressed in meters water equivalent (m w.e.) per square meter. It is the sum of accumulation by

25 precipitation and riming and ablation by runoff and sublimation. Ice melt is only effectively influencing the mass budget if the produced melt water runs off and does not refreeze in the underlying snow or firn pack. Refreezing of rain water below the surface

provides an additional contribution to the glacier's mass budget. Accurate computation of the mass balance of a glacier therefore involves treatment of both surface and subsurface mass fluxes.

4.1 Surface energy balance model

Forced by meteorological input data the energy balance model calculates all energy fluxes that contribute to the surface energy budget. The sum of all fluxes is equal to the energy available for melting (Q_{melt}), as described by the energy balance equation:

$$Q_{melt} = SW_{net} + LW_{net} + Q_{sens} + Q_{lat} + Q_{rain} + Q_{sub}, \tag{1}$$

where SW_{net} is the net shortwave radiation, LW_{net} is the net longwave radiation, Q_{sens} and Q_{lat} are the turbulent sensible and latent heat flux, Q_{rain} is the heat transfer by rainfall, and Q_{sub} is the heat flux into the ice. Fluxes towards the surface are defined as positive. In the model, energy fluxes are formulated such that the surface temperature is the only unknown, which is found by iteratively solving Eq. (1) with the left-hand-side set to zero. In case the computed surface temperature is above melting point, the surface temperature is set to melting point and energy fluxes are recomputed. In that case the sum of fluxes is positive and melting will occur. Next, a brief description of fluxes in the energy balance model will be given. Since the model has been developed along the lines presented by Klok and Oerlemans (2002), the reader is referred to this study for further details.

The amount of solar radiation impinging on the surface depends on multiple factors: the top-of-atmosphere radiation, the transmissivity of the atmosphere, shading by the surrounding terrain, the orientation of the grid cell, the reflectivity of the surrounding terrain and the diffusivity of the sky. Input of cloud cover, air pressure and specific humidity is required to explicitly compute the atmospheric transmissivity due to Rayleigh scattering and gaseous absorption (Kondratyev, 1969), water vapor absorption (McDonald, 1960) and attenuation by aerosols (Houghton, 1954) and clouds. The model distinguishes between direct, diffuse and reflected solar radiation, coming from the

surrounding terrain, and determines every half-hourly time-step whether a grid cell is shaded by the surrounding topography. A half-hourly time-step is used to improve the accuracy in the computation of direct solar radiation, and values are averaged to obtain 3-hourly estimates. The computed amount of outgoing solar radiation is controlled by the formulation of the surface albedo. A parameterisation developed by Oerlemans and Knap (1998) has been adopted, in which the albedo is expressed as a function of the time since the last snow fall event and the snow depth. The calculated amount of incoming longwave radiation from the sky is expressed as a function of cloud cover, air temperature and specific humidity, as described by Konzelmann et al. (1994). The Stefan-Boltzmann law, describing thermal emittance of a blackbody, is used to compute the outgoing longwave radiation. The turbulent sensible and latent heat flux formulations depend on the large-scale temperature and humidity, following the expressions given by Oerlemans and Grisogono (2002). In contrast to the Monin-Obukhov similarity theory, in this approach no knowledge is required of near-surface temperature, humidity and wind characteristics; quantities which are strongly influenced by the ice surface. Despite its small impact on the energy budget, the heat supplied by rain at the ice surface is also considered in the surface heat budget. Finally, the glacier heat flux, which depends on the conductivity of the medium and the vertical temperature gradient, is computed by extrapolation of near-surface heat transport in the subsurface model to the surface.

4.2 Subsurface model

The evolution of vertical profiles of temperature, density and water content on the grid is simulated with a subsurface model, which is based on the SOMARS model developed by Greuell and Konzelmann (1994). SOMARS has been coupled to a distributed energy balance model before by Bougamont et al. (2005) and Reijmer and Hock (2008).

The subsurface temperature evolution is described by the thermodynamic equation:

$$\rho c_p(T)\frac{\partial T}{\partial t} = \frac{\partial}{\partial z}\left(\kappa(\rho)\frac{\partial T}{\partial z}\right) + \frac{F L_M}{\Delta z}, \tag{2}$$

where ρ is the layer density, T is the layer temperature, $c_p(T)$ is the heat capacity of snow/ice, z is the vertical coordinate, Δz is the layer thickness, $\kappa(\rho)$ is the effective conductivity, F is the refreezing rate and L_M the latent heat of melting ($3.34 \times 10^5\,\mathrm{J\,kg^{-1}}$). Expressions for $\kappa(\rho)$ and $c_p(T)$ are taken from Sturm et al. (1997) and Yen (1981), respectively:

$$\begin{aligned}\kappa(\rho) &= 0.138 - 1.01 \times 10^{-3}\rho + 3.23 \times 10^{-6}\rho^2 \\ c_p(T) &= 152.2 + 7.122T\end{aligned} \tag{3}$$

The first term on the right hand side of Eq. (2) represents layer heating by a vertical gradient in the diffusive heat flux, whereas the second term describes heat production by refreezing of water within a layer. Since penetration of shortwave radiation in the upper snow layers is neglected, no subsurface melting may occur. This implies that all water in the snow pack originates from percolation of surface melt water or rain water.

The densification equation describes the time-evolution of the vertical density profile:

$$\frac{\partial \rho}{\partial t} = K_g(\rho,T) + \frac{F}{\Delta z}. \tag{4}$$

Here, $K_g(\rho,T)$ represents gravitational densification, which is computed using a formulation developed by Arthern et al. (2010), based on in situ measurements of Antarctic snow compaction, and recently modified by Ligtenberg et al. (2011):

$$K_g(\rho,T) = C(b)bg(\rho_{ice} - \rho)\exp\left(-\frac{E_c}{RT} + \frac{E_g}{RT_{avg}}\right), \tag{5}$$

where b is the accumulation rate (in $\mathrm{mm\,a^{-1}}$), g is the gravitational acceleration ($9.81\,\mathrm{m\,s^{-2}}$), ρ_{ice} is the density of ice ($917\,\mathrm{kg\,m^{-3}}$), R is the universal gas constant

$(8.314\,\mathrm{J\,mol^{-1}\,K^{-1}}$), and E_c ($= 60\,\mathrm{kJ\,mol^{-1}}$) and E_g ($= 42.4\,\mathrm{kJ\,mol^{-1}}$) are the activation energies associated with creep by lattice diffusion and grain growth, respectively. T_{avg} denotes the temporal mean subsurface temperature and is dynamically computed by taking the mean subsurface temperature of the preceding year. Ligtenberg et al. (2011) introduced the dependence of C on the accumulation rate b, which yields the following formulations of $C(b)$:

$$C(b) = \begin{cases} 0.0991 - 0.0103\log(b), & \text{if } \rho < 550\,\mathrm{kg\,m^{-3}} \\ 0.0701 - 0.0086\log(b), & \text{if } \rho \geq 550\,\mathrm{kg\,m^{-3}} \end{cases}. \tag{6}$$

In case a snow/firn pack is present, the available amount of water at the surface, originating from ice melt and rain fall, will percolate downwards. Refreezing of the percolating water will raise subsurface temperatures and densities. The density cannot exceed the density of ice, whereas the temperature cannot be raised above melting point, which exposes two constraints on the maximum amount of refreezing. In case not all the available percolating water refreezes in a layer, a small amount of water, called irreducible water, will be held by capillary forces while the remaining water percolates into the next layer. In accordance with Schneider and Jansson (2004), an empirical relation has been used to compute the maximum irreducible water content θ_{mi}, i.e. the ratio of the mass of irreducible water to the total mass of the layer, that can be stored in a layer. θ_{mi} is expressed as a function of the porosity n, i.e. the ratio of pore space to the total volume of the snow layer, as follows:

$$\theta_{mi} = 0.0143\exp(3.3n). \tag{7}$$

Downward percolation of water continues until an ice layer is reached. On top of the impermeable ice, water may be stored in the remaining pore space to form a slush layer. In contrast to the irreducible water content, the slush water runs off gradually, resulting in an exponential decay of the slush water content S:

$$S(t) = S(t - \Delta t) \exp\left(\frac{\Delta t}{t^*}\right), \tag{8}$$

where Δt is the model time-step. The time-scale t^* controls the efficiency of the runoff and is expressed as a function of the surface slope β as follows (Zuo and Oerlemans, 1996):

$$t^* = C_1 + C_2 \exp(-C_3 \tan\beta), \tag{9}$$

where C_1, C_2 and C_3 are constants for which values of respectively 0.5, 200 and 133 are similar to those found by Reijmer and Hock (2008). Consequently, the runoff timescale takes values of 200, 20 and 0.5 days for surface slopes of 0, 1 and 5 degrees, respectively. Surface runoff occurs when either bare ice is exposed at the surface or when the slush water level in the firn pack equals the surface height. Under both circumstances, excess water is assumed to runoff instantly. Note that a snow pack effectively delays the runoff of melt water produced at the surface, and hence the vertical transport of water to the base of the ice. Horizontal transport from one grid cell to another is not considered in the model, since this requires explicit treatment of surface flows and vertical drainage through moulins, which is beyond the scope of this study.

4.3 Numerical setup

Numerical experiments are performed on a grid containing 825×646 grid points with a horizontal grid spacing of 40 m. Of these points only 23 %, corresponding to 120 671 grid cells, is assigned to the glacier (Fig. 1). Prior to the start of the time-loop, in which the surface energy balance and subsurface profiles are updated with a 3-h time-step, topographical parameters are determined following a procedure described by Dozier and Frew (1990). These topographical parameters include the terrain view factor, i.e. the fraction of the overlying hemisphere covered by terrain, and the ice fraction, i.e. the fraction of the surrounding visible terrain covered by ice. Both parameters

Title Page

Abstract | Introduction

Conclusions | References

Tables | Figures

|◄ | ►|

◄ | ►

Back | Close

Full Screen / Esc

Printer-friendly Version

Interactive Discussion

are required in the calculation of incoming solar radiation coming from the surrounding terrain and depend strongly on the orientation and location of the grid cell. Topographic shading is time-dependent and evaluated with a half-hour time-step. Note that the glacier geometry is assumed to be invariant in time. Incorporating an evolving geometry would require coupling of the mass balance model to an ice dynamical model. By not considering the geometric evolution, we, among other effects, disregard the impact of the mass balance-height feedback, which enhances surface height fluctuations and may become significant over longer periods of time.

The snow model tracks the evolution of subsurface temperatures, densities and the irreducible and slush water content. A total of 17 vertical layers extending 47 m below the surface is considered with layer depths increasing exponentially from 0.10 m just below the surface to about 10 m for the lowermost layer. After a change in the surface height by snow fall, gravitational densification, ice melt or sublimation/riming, vertical profiles will shift and layer properties are updated accordingly. Diffusion of heat in the snow pack is computed by applying an explicit method, in which forward differencing for the time-derivative and second-order central differencing for the space derivative is used. A sufficiently small time-step of one hour is used to assure stability and convergence of the heat diffusion method in the thin uppermost layers. At the lower boundary of the snow model, no heat transport can occur and the vertical density gradient is set to zero. Fresh snow is added at the top of the snow model with a density ρ_{fs} of 300 kg per m^3, thereby accounting for the rapid densification in the first few hours after a snow event.

4.4 Calibration

Without calibration, the set of model formulations contains several poorly-constrained parameters. Observations on the glacier provide valuable information that can help to reduce the uncertainty in these parameters. In this study, radiative flux observations at the AWS site, Sonic Ranger measurements, snow depth at two stake sites and precipitation data from Svalbard Airport are used to calibrate the model.

In order to calibrate the modelled incoming solar radiation (SW_{in}), AWS measurements in 2009 and 2010 are employed. Observed half-hourly SW_{in} is corrected for the tilt angle of the sensor and averaged to obtain 3-hourly estimates. Two steps are taken to tune the modelled SW_{in}: (1) calibration of the aerosol transmissivity under clear-sky conditions, and (2) inding an expression for the cloud transmissivity as a function of the cloud cover. The aerosol transmissivity, τ_a, can be expressed as a function of the optical air mass m (pressure corrected), following Houghton (1954):

$$\tau_a = k^m, \tag{10}$$

where k is a constant, for which values are typically in the range 0.87–1.00, depending on the geographic position Davies and McKay (1989). We found a value for k of 0.97 by matching the observed SW_{in} under clear-sky conditions to simulated values over the calibration period. The cloud fraction at the AWS site is estimated using a method described by Van den Broeke et al. (2004, 2006) and Kuipers Munneke et al. (2008). This method assumes that at a certain air temperature, LW_{in} is linearly related to the cloud cover. Following Klok and Oerlemans (2002), the cloud transmissivity τ_{cl} is computed by taking the ratio of the observed SW_{in} and the modelled clear-sky SW_{in}. The resulting values of τ_{cl} are assumed to be a function of the cloud fraction and similar to the procedure described by Greuell et al. (1997), a fit has been made to find the following expression for the cloud transmissivity as a function of the cloud fraction n:

$$\tau_{cl} = 1.00 - 0.128\,n - 0.346\,n^2. \tag{11}$$

Comparing Eq. (11) to the expression found by Greuell et al. (1997) for an Alpine glacier, shows that τ_{cl} in Eq. (11) depends less strongly on the cloud fraction, which might be related to geographical differences in the prevailing cloud type and associated optical depth.

The amount of incoming long wave radiation depends on the emissivity of the sky ϵ, which is formulated as a function of the cloud fraction after Konzelmann et al. (1994):

$$\epsilon = \epsilon_{cs}(1 - n^2) + \epsilon_{cl}n^2, \tag{12}$$

with ϵ_{cl} a constant and ϵ_{cs} a function of the vapour pressure, e_a, and air temperature, T_a (Greuell and Konzelmann, 1994):

$$\epsilon_{cs} = 0.23 + b\left(\frac{e_a}{T_a}\right)^{\frac{1}{8}}, \tag{13}$$

5 where b is a constant. In this study, LW_{in} is calibrated by finding values for the constants b and ϵ_{cl} for which discrepancies in the modelled LW_{in} are minimized in respect to observed values. Due to short-circuit problems during the melting season in 2009 and 2010, only longwave radiation measurements outside the melting season are available for comparison. Note that ϵ_{cl} and b can be determined independently by considering 10 cloud-free and fully cloudy conditions. A value for ϵ_{cl} was found by comparing modelled and observed overcast (cloud fraction >95 %) LW_{in} and resulted in a value for ϵ_{cl} of 0.990. A comparison of simulated and observed LW_{in} under clear-sky conditions (cloud fraction <5 %) led to a value for b of 0.447. These values agree well with estimated values for ϵ_{cl} and b of 0.984 and 0.433 by Klok and Oerlemans (2002) for the 15 Morteratsch glacier in Switzerland.

The observed albedo at the AWS site, derived from incoming and reflected shortwave radiation, is employed to constrain values for the ice albedo α_{ice} (0.32), fresh snow albedo α_{fs} (0.87) and to estimate a threshold snow fall rate P_{fs} (0.04 mm w.e. per hour) above which the albedo is set to the albedo of fresh snow.

20 The relative amount of liquid and solid precipitation in the model is determined by the local air temperature. A threshold air temperature, $T_{s/r}$, for which the precipitation is assumed to be half rain and half snow, is derived from time-series of precipitation type and the corresponding air temperature at Svalbard Airport since the year 2000. The resulting value for $T_{s/r}$ is 274.6 K. Around this threshold value the relative fraction 25 of snow fall with respect to the total precipitation is assumed to decrease linearly from 100 % at $T_{s/r} - 1$ K to 0 % at $T_{s/r} + 1$ K.

Snow depth measurements at the sonic ranger site and the AWS site in March 2007 and 2008 are used to tune the altitudinal precipitation gradient, γ_p. This resulted in a yearly mean value for γ_p of 370 mm per km. With this gradient, the maximum precipitation of 0.54 m w.e. per year (Pälli et al., 2002) is reached at 971 m a.s.l.

The turbulent flux formulations, adopted from Oerlemans and Grisogono (2002), include a background exchange coefficient C_b, associated with turbulence generated by the large-scale wind. Lacking direct observations of turbulent fluxes, a value for C_b of 0.0028 has been estimated by matching simulated snow and ice melt in 2007 to observations at the Sonic Ranger site. Note that calibration of C_b and γ_p should be done after calibration of the other tuning parameters, since ice melt and snow depth do not vary independently of the setup of the other tuning parameters. We chose to tune γ_p before calibrating C_b, since the influence of C_b on snow depth is much less pronounced than the impact of γ_p on ice melt.

4.5 Initialisation

Subsurface profiles of density, temperature and water depend strongly on the history of the subsurface processes and the surface forcing. Due to the significance of vertical advection and diffusion in mass and heat transport, the response time of subsurface variables increases rapidly with distance from the source of variability (mainly at the surface). At a depth equivalent to the maximum depth in the snow model (±47 m), the response time is typically in the order of a few decades. It is therefore important to have properly initialised subsurface profiles at the start of the model run in 1989. To do so, observed snapshots of the vertical borehole temperatures at the drill site in May 1997 are employed and serve as benchmark against which the initial profiles are calibrated. The strategy of the initialisation procedure is to loop the model over the period 1989–1997 as often as is required to resemble the observed borehole temperature profile. Note that the drill site is not part of the selected grid of Nordenskiöldbreen, where the surface energy budget and vertical profiles are computed every model time-step (Fig. 1). Nevertheless, for initialisation purposes the surface energy balance and

Melt, runoff and refreezing on Nordenskiöldbreen

W. J. J. van Pelt et al.

Title Page

Abstract | Introduction

Conclusions | References

Tables | Figures

◄ | ►

◄ | ►

Back | Close

Full Screen / Esc

Printer-friendly Version

Interactive Discussion

evolution of the snow pack has been simulated for the grid point nearest to the drill site as well. At the start of the first loop of initialisation, linear vertical density profiles are prescribed, whereas vertical temperatures are set equal to an arbitrary value of 265 K. The initial snow depth is set to increase linearly with altitude from 0 m at 700 m a.s.l. to 25 m at the altitude of the drill site (1237 m a.s.l.).

Figure 3 shows subsurface densities and temperatures at the location of the drill site after every 8 yr loop of the initialisation procedure. Observed subsurface temperatures (Van de Wal et al., 2002) and densities (Pohjola et al., 2002b) at the drill site in May 1997 are also shown. Best agreement between modelled and observed subsurface temperatures is found after 32 yr of initialisation. The initial vertical profiles at the start of the fourth initialisation loop are used as reference profiles for the entire grid in May 1989. Discrepancies in the simulated temperatures in the upper 12 m of the snow pack could be related to an overestimation of modelled accumulation. Pälli et al. (2002) found a relatively small accumulation rate at the top of the ice cap in comparison with the higher parts of the glacier and ascribed this difference to the effect of wind-driven snow transport. Note that the temperature at great depth is much higher than the yearly mean air temperature at this altitude of $\pm -12\,°C$, which demonstrates the significance of refreezing. In contrast to the simulated densities, the observed density profile shows a large variability between the different layers (Fig. 3). Simulating small-scale density variations would require a more detailed treatment of the evolution of the snow microstructure, melt water percolation and a higher vertical model resolution.

The aforementioned initialisation procedure requires calibrated values of the tuning parameters. Therefore, the calibration procedure in Sect. 4.4 is performed prior to the initialisation with tuned values of the calibration parameters. Since accurate calibration of γ_p and C_b requires initialised subsurface profiles as well, calibration experiments with various setups of γ_p and C_b start already in 1989 (18 yr prior to the start of the actual calibration period in 2007). Note that the calibration of k, ε_{cl} and b does not require initialised subsurface profiles, since the snow properties do not affect the modelled incoming shortwave and longwave fluxes.

5   Standard run: 1989–2010

Starting from initialised subsurface profiles, a 21-yr simulation is performed covering the period from October 1989 to October 2010. In this section, we present the temporal evolution and spatial distribution of the mass and energy balance and discuss these in relation to evolving subsurface properties.

5.1   Mass and energy budget

Figure 4 presents contour plots of the annual mean mass balance, refreezing and runoff, averaged over the full simulation period. Spatial variations in the mass balance are to a large extent explained by a combination of altitudinal differences in air temperature and precipitation, spatial gradients in the surface albedo and local variations in the amount of refreezing. Local mass balance variations by topographic effects are only significant in the immediate vicinity of steep valley walls. The equilibrium line altitude over the simulation period is on average 719 m a.s.l. Over the period spanned by the stake measurements (2006–2010), the observed ELA is ±600 m a.s.l. This is somewhat lower than the simulated ELA over the same period of 631 m a.s.l. The mean net mass balance for 1989–2010 is −0.39 m w.e. per year. As grid boundaries are selected along the ice divide, no ice is assumed to flow into the model domain. In order to compute the actual mass budget of the glacier, the negative contribution of calving should be considered in the mass budget as well. This term is likely to be small, since the glacier snout has almost fully retreated on land over the course of the simulation period.

   Refreezing of subsurface water is most significant in the accumulation zone, where percolating and stored water refreezes down to tens of meters below the surface. In the accumulation zone, low snow temperatures at the start of the melting season increase the potential for refreezing. Despite high melt rates in the ablation zone, refreezing is limited by the disappearance of snow during the melt season. A maximum in the amount of refreezing is found around 1000 m a.s.l. On average, refreezing contributes

Melt, runoff and refreezing on Nordenskiöldbreen

W. J. J. van Pelt et al.

0.27 m w.e. per year to the mass budget. Hence, 25 % of all melt water (1.05 m w.e. a^{-1}) and rain water (0.05 m w.e. a^{-1}) at the surface refreezes in the snow pack. Refreezing is equivalent to 69 % of snow accumulation during a year. Runoff of water is mainly controlled by the melt rate and the amount of refreezing. In the accumulation zone, a

5　large fraction of the available water at the surface refreezes in the snow pack, thereby limiting the amount of runoff of slush water. Averaged over the glacier the net runoff is 0.82 m w.e. a^{-1} per unit area, implying a total annual discharge of 1.58×10^8 m^3.

　　The mass balance is a product of precipitation, runoff and latent transport by sublimation and riming. Figure 5 shows height-profiles of the mass budget and its defining

10　components. The mass exchange with the atmosphere by sublimation and riming is negligibly small, so the sum of precipitation and (negative) runoff determines the mass budget. High up in the accumulation zone, melt occurs while runoff goes to zero, which implies that all ice melt refreezes. Precipitation dominates the mass budget at high altitudes, whereas ice melt dominates the mass budget in the ablation zone. The mean

15　altitudinal mass balance gradient in the ablation zone is 4.1 mm w.e. a^{-1} m^{-1}, which is approximately similar to the average found for Svalbard by Hagen et al. (2003).

　　Contour plots of the components that comprise the energy budget are shown in Fig. 6. The energy involved in melting (Fig. 6a), i.e. the sum of all the incoming and outgoing fluxes, decreases with altitude and is very small in the accumulation zone,

20　although some melting occurs even at the highest point on the grid. The net short-wave flux (Fig. 6b) is the main source of energy at the surface and its spatial pattern is to a large extent controlled by the surface albedo. Generally, the effect on the short-wave budget of shading near valley walls is relatively small. The net longwave flux (Fig. 6c) is the main energy sink and is strongly dependent on the temperature deficit

25　at the surface, which increases with altitude. Regarding the turbulent fluxes (Fig. 6d), the sensible heat flux contributes significantly to the energy budget, whereas the latent heat flux is small. Due to refreezing, the subsurface heat flux (Fig. 6e) is positive and contributes significantly to the surface heat budget, especially in the accumulation zone. Surface cooling due to a high surface albedo in the accumulation zone is

therefore partly compensated by an enhanced subsurface heat flux towards the surface. Surface heating by rain fall (Fig. 6f) is of negligible magnitude.

Time-series of the net mass balance, runoff and precipitation are shown in Fig. 7a. As mentioned before, the net mass balance almost equals the sum of runoff and precipitation. Over the simulation period, two positive mass balance years occurred (1992 and 1996), which are also the years with the lowest runoff. The large inter-annual variability is explained by strong year-to-year variations in summer melt and snow depth. The most negative net mass balance of $-0.95\,\mathrm{m\,w.e.\,a^{-1}}$ is found in 1998, which is related to high summer temperatures in combination with limited snow fall during the preceding winter season. Annual mean temperatures in Fig. 7d reveal a positive trend in annually averaged air temperatures since 1989, whereas this trend is not clear for summer mean air temperatures. This finding is in line with observed seasonal temperature trends at Svalbard Airport since 1912, which reveal a preferred warming outside the summer months (Hanssen-Bauer et al., 2009). Correlations of -0.66 and 0.64, significant at a 99 %-confidence level, exist between net mass balance and summer mean air temperature and annual precipitation, respectively. A correlation of only -0.10 is found between the net mass balance and annual mean temperatures, which demonstrates the insignificance of temperature variations outside the melt season on the mass budget. Winter snow fall is significant, owing to both its direct effect on the surface mass budget and the impact on the length of the melt season. Time-series of the annual amount of refreezing in Fig. 7b reveal a modest year-to-year variability over the simulation period. The variability is mainly resulting from fluctuations in annual snow fall, having a major impact on refreezing in the ablation area, and air temperature, which affect the cold content of the snow pack and the amount of melt available for refreezing in the accumulation zone. Figure 7c shows a comparison of the net mass balance time-series with observed mass balance records for Kongsvegen (western Svalbard) and Hansbreen (southern Svalbard), provided by the World Glacier Monitoring Service (WGMS). Correlations of 0.79 and 0.56 are found between the simulated mass balance and records at Kongsvegen and Hansbreen, respectively. The simulated mean mass

balance is 0.30 m w.e. higher for Kongsvegen and 0.05 m w.e. higher for Hansbreen, but both are also negative on average since 1990.

5.2 Subsurface variables

Figure 8a and b shows time-series of the vertical temperature and density distribution for the period 1989–2010 at stake site S9, which is located in the accumulation zone (just above the ELA). Furthermore, focussed time-series for the year 2009, additionally showing the irreducible and slush water content, are presented in Fig. 8c–f. Surface melt percolates into the snow pack and subsequent refreezing heats the snow to melting point in summer. This continues until the percolating water encounters the impermeable ice and starts to form a slush layer. Heat diffuses into the underlying cold ice and after the melting season a cold wave penetrates into the firn pack from above, causing the stored slush water and irreducible water to refreeze gradually. Subsurface temperatures remain at melting point until the water content of a layer is entirely depleted. The inter-annual variability in refreezing at S9 is quite large and determined by both surface melt water production and the cold content of the snow pack. Note that the snow depth reaches a minimum between 2004 and 2006, thereby limiting the amount of refreezing during this period. Figure 8 also shows the delayed response of ice temperatures with depth to the forcing at the snow-ice interface.

An example of simulated runoff time-series at S6 in the ablation zone for the year 2010 are shown in Fig. 9. Surface melting starts in early May and until early June all melt water refreezes and runoff is absent. From then on, a slush layer is formed and water runs off gradually until the snow pack has fully melted. Clearly, the snow pack has a buffering effect on the amount of runoff. Only when the snow pack is gone all available water at the surface runs off immediately, which induces a clear diurnal cycle. A snow fall event in August shuts down ice melt and runoff for several days, which has a remarkable impact on the mass budget as demonstrated by Oerlemans and Klok (2004) for a summer snow fall event on the Morteratschgletscher, Switzerland. A

Title Page

Abstract | Introduction

Conclusions | References

Tables | Figures

◄ | ►

Back | Close

Full Screen / Esc

Printer-friendly Version

Interactive Discussion

Title Page

Abstract | Introduction

Conclusions | References

Tables | Figures

◄ | ►

◄ | ►

Back | Close

Full Screen / Esc

Printer-friendly Version

Interactive Discussion

limited amount of snow fall in summer leads to a major increase in the albedo and thus effectively reduces the amount of absorbed solar radiation and thus melt.

Along the cross-section marked in Fig. 1, vertical profiles of mean subsurface temperatures and densities over the final year of simulation (2009–2010) are presented in Fig. 10. Around the ELA, a clear transition from cold ice in the ablation area to temperate snow/firn in the accumulation zone is seen. In the accumulation zone, heating by refreezing dominates advection and diffusion of lower surface temperatures at depths >5 m. In the ablation area, refreezing in the shallow snow pack during the melting season raises near-surface temperatures. Temperatures at the base of the vertical domain in the ablation zone are a measure for the mean temperature at the snow-ice interface over several decades as vertical heat diffusion is a slow process. Hence, in a changing climate this induces a buffering effect as slowly changing subsurface temperatures have a longterm impact on the subsurface heat flux at the surface. It should be noted that a zero energy flux at the lower boundary of the vertical domain might be a crude assumption in the ablation area where likely warmer ice gets advected from below. Note that inclusion of horizontal advection of ice by ice flow would lead to a horizontal shift, increasing with depth, of the vertical profiles in Fig. 10. A near-surface temperature distribution with temperate ice in the accumulation zone and cold ice near the surface in the ablation zone is typical for glaciers in Svalbard (Blatter and Hutter, 1990; Pettersson, 2004).

5.3 Comparison with observations

As mentioned in Sect. 4.4, extrema in observed SW_{in}, SW_{out}, and LW_{in} at the AWS between March 2009 and November 2010 are used to calibrate modelled fluxes. Scatter plots of the latter fluxes, presented in Fig. 11, show a good agreement between the modelled and measured values with correlation coefficients between 0.83 and 0.91. Discrepancies of simulated SW_{in} are mainly resulting from errors in the estimated cloud cover, which is also reflected in discrepancies in LW_{in}. Recall that due to short-circuiting problems we lack observations of longwave fluxes during the melting season.

The net shortwave and longwave budgets are on average overestimated by $1.6\,\mathrm{W\,m^{-2}}$ and $1.9\,\mathrm{W\,m^{-2}}$, respectively. The only non-calibrated flux is the outgoing longwave radiation. Modelled values of LW_{out} agree well with observations ($R = 0.93$), which is an indication that modelled surface temperatures are reasonably accurate. Recall that the
5 surface temperature is the only unknown in the energy balance equation.

Validation of the surface mass balance is performed by comparing modelled values to stake observations. The observed surface height variations are converted into mass changes by employing the mean observed snow density in snow pits in 2008 and 2009 of $372\,\mathrm{kg\,m^3}$. Figure 12 reveals a good agreement between measured and simulated
10 mass balance values for S3–11. At S1 and S2, the model overestimates mass loss, which could be related to wind-driven snow transport accumulating mass in this area. Figure 1 illustrates that, in contrast to S3–11, stakes S1 and S2 are positioned close to the southern edge of the ice grid in the vicinity of steep valley walls.

Finally, we compare observed snow temperatures and densities in snow pits in spring
15 2008 and 2009 to simulated values. For that purpose, seven observed vertical profiles are adopted and vertically averaged values over the full depth of the snow pack in the ablation area are compared to modelled mean values (not shown). The mean measured snow temperature of $256.2\,\mathrm{K}$ is only $0.5\,\mathrm{K}$ lower than the simulated mean. In comparison to the mean measured density, the simulated mean snow density of
20 $349\,\mathrm{kg\,m^{-3}}$ is $18\,\mathrm{kg\,m^{-3}}$ lower than observed. Besides uncertainty in the simulated densification rate, this discrepancy may also be related to an underestimation of the fresh snow density.

6 Sensitivity experiments

Additional experiments are performed to test the model sensitivity to changes in model
25 parameters (Sect. 6.1), initial conditions (Sect. 6.2) and climate (Sect. 6.3).

6.1 Parameter sensitivity

A set of 5-yr runs over the period 2005–2010 is performed to investigate the robustness of the model output to changes in model parameters. An overview of the sensitivity of the mass balance, refreezing and runoff averaged over the glacier to perturbations of selected model parameters is given in Table 1. The simulated mass balance and runoff is most sensitive to changes in parameters that affect the net shortwave budget (α_{ice}, α_{fs}, k, γ_p, P_{fs} and $T_{s/r}$) and longwave radiative budget (ϵ_{cl} and b). Especially, the sensitivity to perturbations of the fresh snow albedo (α_{fs}) is high, since the relative impact on the shortwave budget is large. The amount of refreezing is mainly sensitive to changes in parameters that affect the surface temperature (C_b), snow thickness (γ_p) and snow density (ρ_{fs}). The rate at which slush water runs off is controlled by the parameter C_{ro}, which is a scaling factor for the runoff time-scale. Despite its impact on the runoff rate, perturbing C_{ro} has only a limited effect on the net mass balance, refreezing and runoff. A clear nonlinear response of the mass balance to changes in the maximum accumulation rate a_{max} is explained by a nonlinearity in the area affected by a change in a_{max}. An upward shift of the altitude at which maximum accumulation is reached affects only a very small portion of the grid as a relatively small amount of grid points is located above 1000 m a.s.l.

6.2 Initialisation sensitivity

The relevance of extensive initialisation is investigated by perturbing initial subsurface profiles. For that purpose, two simulations over the period 2004–2010 are performed with the initial water content in the snow pack set to zero in both simulations and the subsurface temperature reduced by 3 K in one of the runs. Reducing the subsurface temperatures by 3 K induces a mass balance sensitivity to +27 mm w.e. after 1 yr and +60 mm w.e. between 2–6 yr since the start of the experiment. It can be concluded that lowering subsurface temperatures has only a modest but long-term effect on the

mass balance and we therefore conclude that highly-accurate simulation of the mass balance requires properly initialised subsurface conditions.

6.3 Climate sensitivity

In order to study the mass balance sensitivity to future changes in climate, we performed multiple runs with perturbed air temperature T and precipitation P over the period 2000–2010. Statistical downscaling of GCM future climate scenarios for Svalbard has indicated a strong seasonal variability in climate change with more pronounced warming in winter and spring (Benestad, 2008; Førland et al., 2009). In one set of runs, T and P perturbations are evenly distributed over the seasons, whereas in a second set of experiments unevenly distributed climate variations are prescribed. The degree of inhomogeneity of climate change throughout the year is based on future estimates of the seasonal mean T and P at Svalbard Airport for the period 2070–2100 (Førland et al., 2009). Future downscaled GCM estimates are based on the A1b-emission scenario (IPCC, 2001). Observational data from Svalbard Airport over the period 1980–2010 are used to compute mean seasonal T and P in 1995, which serve as reference values. Hence, by taking the difference of seasonal T and P between 1995 and 2085, the relative change per season with respect to the annual mean change is calculated. The related scaling factors for temperature change in winter, spring, summer and autumn are 1.48, 1.45, 0.39 and 0.68, respectively. Scaling factors for precipitation perturbations are 1.61, 1.06, 1.07 and 0.27 for winter, spring, summer and autumn. These scaling factors are used in the seasonally inhomogeneous climate sensitivity experiments (2000–2010) to scale T and P perturbations per season.

The net mass balance sensitivity to T and P perturbations with and without seasonality is presented in Table 2. Altitudinal mass balance sensitivity profiles for eight of the seasonally invariant climate change experiments are shown in Fig. 13. Clearly, the mass balance responds nonlinearly to changes in T and P. Figure 13 illustrates that the mass balance is mainly sensitive to climate variations in the ablation zone, where a lower mean surface albedo enhances the melt sensitivity. Climate perturbations lead to

Melt, runoff and refreezing on Nordenskiöldbreen

W. J. J. van Pelt et al.

a shift in the ELA and thus the extent of the ablation zone, thereby explaining the non-linearity. On average a 1 K temperature change is compensated by a 32 % change in precipitation of similar sign in case of seasonally invariant perturbations. On the other hand, in case of seasonally dependent climate change, a 1 K change in temperature is balanced by a smaller change in precipitation of 17 %. Note that including seasonality has a small effect on the mass balance sensitivity to precipitation perturbations. This can be expected, since enhanced precipitation in winter and reduced precipitation in autumn hardly affects the snow depth at the start of the melting season. On the other hand, incorporating seasonality has a major impact on the mass balance sensitivity to temperature perturbations. Since the mass balance is mainly a product of melt in the summer months and yearly precipitation, the reduced increase of summer temperatures has a pronounced effect on the mass balance sensitivity. This stresses the importance of considering climate change on a seasonal scale, especially in regions like the Arctic where temperature increase is expected to be less pronounced during the melting season.

In additional runs, T or P is perturbed for one season, while unperturbed values are used for the other seasons. In this way the sensitivity of the annual mass balance to seasonal climate variations can be estimated. In a similar fashion, monthly variations can be used to construct a seasonal sensitivity characteristic (Oerlemans and Reichert, 2000). Figure 14 shows the mass balance sensitivity to various seasonal T and P changes. The mass balance sensitivity to T variations is pronounced in summer, whereas in winter the impact is negligible. Seasonal P perturbations have a year-round impact on the annual mass balance.

7   Extending mass balance time-series

The outcome of the sensitivity experiments in Sect. 6.3 contains useful information on the sensitivity of the total mass balance under altered climatic conditions. The simulated mass balance sensitivities for 2000–2010 can be employed to extend the mass

Title Page

Abstract | Introduction

Conclusions | References

Tables | Figures

◄◄ | ►►

◄ | ►

Back | Close

Full Screen / Esc

Printer-friendly Version

Interactive Discussion

W. J. J. van Pelt et al.

Title Page

Abstract Introduction

Conclusions References

Tables Figures

◄◄ ►►

◄ ►

Back Close

Full Screen / Esc

Printer-friendly Version

Interactive Discussion

balance time-series in the past and future when the T and P evolution is prescribed. It is assumed that the sensitivity to a simultaneous change in P and T is equivalent to the sum of both sensitivities. Note that this assumption regards the sensitivities to T and P perturbations as independent quantities (not T and P itself).

First we extend the mass balance time-series back in time. Seasonal sensitivity data, of which a selection is presented in Fig. 14, are used to construct functions per season of the mass balance versus T and P perturbations. Polynomial curve fitting is performed to express the net mass balance as a function of T and P perturbations for the four seasons. For the period 1912–1989, time-series of seasonal mean T and P values are derived from monthly composite time-series at Svalbard Airport (Hanssen-Bauer et al., 2009). The time-series are scaled to match the simulated gridded mean for Nordenskiöldbreen for 1990–2010. The resulting T and P records are then used to compute the seasonal mass balance. Summing the seasonal contributions then yields annual mass balance estimates since 1912.

A similar strategy is employed to extend the mass balance time-series in the future. The annual climate sensitivity data in Table 2 are adopted to derive expressions of the future net mass balance, the amount of refreezing and ELA as a function of changes in T and P. The corresponding fitted curves for the experiments with seasonal variations in climate change are shown in Fig. 15. Similar fits are constructed for the seasonally invariant scenario. Using the derived expressions in combination with a future T and P scenario, time-series of the net mass balance, refreezing and ELA are constructed. Future T and P time-series since 2011 are derived by linearly interpolating between annual mean observed values at Svalbard Airport for 1990–2010 and projected annual mean values in 2085 (Førland et al., 2009). Once again, T and P records for Svalbard Airport are scaled to match the simulated mean for Nordenskiöldbreen for 1990–2010. The adopted scaling factors to account for seasonal inhomogeneity in climate change are given in Sect. 6.3. We assume the degree of inhomogeneity in climate change throughout the year to be constant in the future and therefore the sensitivity to season-ally scaled annual perturbations of T and P in Table 2 could be used.

Melt, runoff and refreezing on Nordenskiöldbreen

W. J. J. van Pelt et al.

Concatenation and integration of the reconstructed (1912–1989), simulated (1990–2010) and projected net mass balance produces the cumulative mass balance time-series over the period 1912–2085, presented in Fig. 16. In addition to the seasonally varying and invariant projections, the projected cumulative mass balance in a constant climate with respect to the period 1990–2010 is given. Figure 16 further shows the projected evolution of cumulative refreezing and the ELA. For 1912–2010, we find a cumulative mass loss of 18 m w.e. The mass loss of 8 m w.e. over the model period (1990–2010) can be related to high summer air temperatures. A positive cumulative mass budget in the 60's and 70's is associated with low summer temperature, whereas mass loss prior to 1940 is associated with a combination of high summer temperatures and reduced accumulation. Accumulation time-series extracted from the 1997 ice core drilled at Lomonosovfonna, presented in Pohjola et al. (2002a), confirm that the mean accumulation rate over the period 1912–1950 was significantly lower (0.10 m w.e. a^{-1}) than over the period 1951–1989. It should be noted that due to a lack of observations at Svalbard Airport prior to 1957, there is a considerable uncertainty in precipitation estimates, thereby reducing the accuracy of mass balance estimates over this period. In a non-changing future climate w.r.t. the period 1990–2010, the projected cumulative mass loss is 29 m w.e. in 2085. If we instead prescribe a seasonally dependent future climate scenario then cumulative mass loss increases to 61 m w.e. A more dramatic scenario arises when we do not account for seasonal variability in climate change, in which case the cumulative mass budget in 2085 is equivalent to −85 m w.e. The cumulative refreezing scenarios in Fig. 16 indicate that refreezing is rather insensitive to climate change; the no-climate-change scenario nearly overlaps with the seasonally varying projection. Figure 15 shows that refreezing increases with an increase in precipitation and decreases with temperature. Hence, in a future climate, the mass balance effect due to refreezing by warming and enhanced precipitation will to a large extent compensate each other. Incorporating seasonality in climate change reduces the projected ELA in 2085 from 1126 m a.s.l. in case of seasonally invariant climate change to 896 m a.s.l.

It should be noted that changes in the surface height and the interaction with ice dynamics are not considered here. Significant surface lowering in the course of time will induce a more negative mass balance as surface air temperatures increase. Furthermore, changes in the glacier area affect the net mass budget, whereas changes in the grid orientation affect the amount of incoming solar radiation. Additionally, enhanced runoff affects subglacial water pressures, which influences basal dynamics and indirectly the surface evolution. Finally, it should be noted the mass balance effect of longterm trends (>10 yr) in subsurface conditions are not captured in the relatively short period of the sensitivity experiments. When regarding the mass balance – height feedback as the most significant omission, the presented mass balance scenarios are likely somewhat cautious estimates.

8   Conclusions and discussion

In an attempt to simulate the surface mass budget of Nordenskiöldbreen, including refreezing and runoff, a distributed surface energy balance model, developed along the lines presented by Klok and Oerlemans (2002), is coupled to a multi-layer snow model, based on the SOMARS model (Greuell and Konzelmann, 1994). Gridded climate input is generated from regional climate model (RACMO) output in combination with meteorological time-series from Svalbard Airport. A best parameter setup is found after calibration with observations on the glacier and at Svalbard Airport. Prior to the actual simulation over the period 1989–2010, extensive initialisation of subsurface profiles is performed to find initial subsurface conditions that evolve to observed borehole profiles in 1997.

Over the period 1989–2010, the simulated net surface mass balance is -0.39 m w.e. a^{-1} with extrema of $+0.17$ and -0.95 m w.e. a^{-1} for mass balance years 1991–1992 and 1997–1998, respectively. Year-to-year variations are explained by fluctuations in summer air temperatures and winter snow fall. Refreezing of subsurface water amounts to 0.27 m w.e. a^{-1}, which is equivalent to 69 % of the annual snow accumulation. The mean simulated ELA is 719 m a.s.l. The net runoff per unit area is

Melt, runoff and refreezing on Nordenskiöldbreen

W. J. J. van Pelt et al.

the sum of discharge of slush water and surface runoff and is equal to 0.82 m w.e. a^{-1}. Refreezing delays and reduces runoff especially in the accumulation zone, where refreezing is most pronounced. The simulated thermodynamic structure is characterised by a temperate accumulation zone (at depths $>\pm 5$ m) and cold ice in the ablation zone.

5 Large amounts of refreezing in the accumulation zone are a consequence of low annual mean temperatures ($<-10\,^\circ$C in the accumulation zone), providing a large cold content in the snow/firn pack at the start of the melting season, in combination with significant melt during the summer season. On the other hand, in the ablation area annual snow accumulation mainly controls the amount of refreezing.

10 Modelled energy fluxes are validated against AWS measurements on the glacier and a generally good agreement is found. Discrepancies are mainly related to uncertainties in the cloud cover input, which affects both shortwave and longwave estimates. A comparison of mass balance estimates from stake observations to simulated values shows a good agreement, except for the two lowest stake locations. We hypothesise

15 that this is related to disregardance of the effect of wind driven snow transport. Snow pit profiles in the ablation zone indicate that simulated snow temperatures correlate well with observations, whereas the density is somewhat underestimated, which is shown to have a very limited impact on the mass balance.

Parameter sensitivity experiments show a high sensitivity of the mass balance and

20 runoff to parameters affecting the shortwave and longwave radiative budget. In particular, the sensitivity to perturbations of the fresh snow albedo is large. The amount of refreezing is sensitive to changes in parameters that affect the surface temperature, snow thickness and snow density. Experiments with perturbed initial subsurface conditions show that the simulated mass balance is modestly affected by changes in

25 initial subsurface temperatures. Nevertheless, the long term influence gives rise to substantial initialisation for accurate simulation of the mass budget.

Multiple climate perturbation experiments are performed and show a non-linear response of the mass balance, refreezing and runoff to changes in temperature and precipitation. Including seasonal variations in climate change, based on a future climate

Melt, runoff and refreezing on Nordenskiöldbreen

W. J. J. van Pelt et al.

scenario for Svalbard Airport, reduces the mass balance sensitivity, mainly as a result of less pronounced summer warming. The simulated sensitivities are employed to derive expressions for the mass balance, refreezing and the ELA as a function of temperature and precipitation perturbations, which are used in combination with past and future temperature and precipitation time-series to compute the mass budget of Nordenskiöldbreen over the period 1912–2085. An advantage of this approach is that it avoids running the model over the actual period under consideration, whereas it does account for varying sensitivities of the mass balance, refreezing and the ELA in a changing climate. Over the period 1912–2010, a cumulative mass loss of 18 m w.e. is found. The computed cumulative mass budget for 2011–2085 is −85 m w.e. and −61 m w.e. for the experiments excluding and including seasonal variations in climate change, respectively. Incorporating seasonality reduces the rise of the ELA and leads to an estimated value of 896 m a.s.l. in 2085. Compensating effects of temperature and precipitation changes cause the amount of refreezing in the future to hardly change in a seasonally varying climate scenario.

Many factors lead to uncertainties in the model output, of which probably the largest source of error is in the model input. One of the main uncertainties in the model forcing is related to spatial and temporal variability in snow accumulation. In the model, the accumulation rate increases linearly with height (at a rate γ_p) and maximizes at a_{max}. In reality, wind patterns will have a major impact on the spatial distribution of the accumulation rate. As discussed by Berthier et al. (2010), a redistribution of snow by wind often leads to enhanced thinning rates along the centerline and additional accumulation in concave areas near the margins. Additionally, temporal variability in γ_p will also have a considerable impact on the simulated mass balance. Accumulation rates along a horizontal profile in the accumulation zone of Nordenskiöldbreen, presented by Pälli et al. (2002), confirm that the accumulation rate varies significantly in space. Errors in the cloud cover estimates, derived from observations at Svalbard Airport, have a significant impact on the modelled shortwave and longwave budget. A comparison of observed air temperatures at the AWS site and RACMO derived temperatures shows a high

correlation and systematic errors for this specific site are found to be small. In absence of sufficient meteorological time-series near the glacier, output of RACMO therefore provides valuable data to force the model. Uncertainties in the simulated mass balance distribution are additionally related to unmodelled effects, like wind-driven snow drift and dust deposition. Regarding the subsurface profiles uncertainties arise from the zero energy flux assumption at the base of the vertical domain, the limited amount of subsurface layers and disregarding horizontal advection of heat, mass and water. Multiple factors lead to errors in the future mass balance, refreezing and ELA predictions, of which neglecting the interaction between the mass balance and surface height and related changes in the ice dynamics are likely most relevant.

Finally, it is worth mentioning that output fields of the subsurface evolution may serve as surface boundary input for an ice dynamical model. Realistically simulating the geometric evolution of a glacier requires dynamic coupling of an ice flow model to a surface model that provides details on the water input, surface temperature and the mass balance. Basal sliding velocities at the ice-bedrock interface are known to depend strongly on the rate of water input from the surface (Zwally et al., 2002; Van de Wal et al., 2008; Schoof, 2010). Refreezing in the snow and firn pack at the start of the melting season effectively delays water transport to the base and hence affects the timing of speed-up events, like observed during the onset of the melting season on Nordenskiöldbreen (Den Ouden et al., 2010). This demonstrates the importance of incorporating a surface mass balance model that accounts for refreezing in order to model ice velocities at seasonal time-scales and smaller.

References

Arthern, R., Vaughan, D., Rankin, A., Mulvaney, R., and Thomas, E.: In situ measurements of Antarctic snow compaction compared with predictions of models, J. Geophys. Res., 115, F03011, doi:10.1029/2009JF001306, 2010. 221

5 Benestad, R.: Empirical-Statistical downscaled Arctic Temperature and Precipitation Series, Met.no Report 12/2008, 2008. 236

Berthier, E., Schiefer, E., Clarke, G., Menounos, B., and Rémy, F.: Contribution of Alaskan glaciers to sea-level rise derived from satellite imagery, Nat. Geosci., 3, 92–95, 2010. 242

Blatter, H. and Hutter, K.: Polythermal conditions in Arctic glaciers, J. Glaciol., 37, 261–269, 10 1990. 233

Bougamont, M., Bamber, J., and Greuell, W.: A surface mass balance model for the Greenland Ice Sheet, J. Geophys. Res., 110, F04018, doi:10.1029/2005JF000348, 2005. 220

Braithwaite, R. and Zhang, Y.: Modelling changes in glacier mass balance that may occur as a result of climate changes, Geogr. Annal., Phys. Geogr., 81, 489–496, 1999. 212

15 Davies, J. and McKay, D.: Evaluation of selected models for estimating solar radiation on horizontal surfaces, Solar Energy, 43, 153–168, 1989. 225

De Woul, M. and Hock, R.: Static mass-balance sensitivity of Arctic glaciers and ice caps using a degree-day approach, Ann. Glaciol., 42, 217–224, 2005. 212

den Ouden, M. A. G., Reijmer, C. H., Pohjola, V., van de Wal, R. S. W., Oerlemans, J., and Boot, 20 W.: Stand-alone single-frequency GPS ice velocity observations on Nordenskiöldbreen, Svalbard, The Cryosphere, 4, 593–604, doi:10.5194/tc-4-593-2010, 2010. 215, 243

Dozier, J. and Frew, J.: Rapid calculation of terrain parameters for radiation modeling from digital elevation data, Geosci. Remote Sens., IEEE Transactions, 28, 963–969, 1990. 223

Ettema, J., van den Broeke, M. R., van Meijgaard, E., van de Berg, W. J., Box, J. E., and 25 Steffen, K.: Climate of the Greenland ice sheet using a high-resolution climate model – Part 1: Evaluation, The Cryosphere, 4, 511–527, doi:10.5194/tc-4-511-2010, 2010. 216

Førland, E., Benestad, R., Flatøy, F., Hanssen-Bauer, I., Haugen, J., Isaksen, K., Sorteberg, A., and Ådlandsvik, B.: Climate development in North Norway and the Svalbard 10 region during 1900–2100, Norsk Polarinstitutt Rapportserie nr. 128, 2009. 214, 236, 238

30 Fountain, A.: Effect of snow and firn hydrology on the physical and chemical characteristics of glacial runoff, Hydrol. Process., 10, 509–521, 1996. 213

Greuell, W.: Hintereisferner, Austria: mass-balance reconstruction and numerical modelling of

the historical length variations, J. Glaciol., 38, 233–244, 1992. 212

Greuell, W. and Konzelmann, T.: Numerical modelling of the energy balance and the englacial temperature of the Greenland Ice Sheet. Calculations for the ETH-Camp location (West Greenland, 1155 m asl), Glob. Planet. Change, 9, 91–114, 1994. 213, 220, 226, 240

5 Greuell, W. and Oerlemans, J.: The evolution of the englacial temperature distribution in the superimposed ice zone of a polar ice cap during a summer season, in: Glacier fluctuations and climatic change: proceedings of the Symposium on Glacier Fluctuations and Climatic Change, held in Amsterdam, 1–5 June 1987, Springer, 6, p. 289, 1989. 213

Greuell, W., Knap, W., and Smeets, P.: Elevational changes in meteorological variables along
10 a midlatitude glacier during summer, J. Geophys. Res., 102, 25941–25954, 1997. 225

Hagen, J., Kohler, J., Melvold, K., and Winther, J.: Glaciers in Svalbard: mass balance, runoff and freshwater flux, Polar Res., 22, 145–159, 2003. 230

Hanssen-Bauer, I., Førland, E., Johansen, K., and Nordli, Ø.: The Climate of Svalbard and Jan Mayen, Analyses of time-series data from 1911 to 2007, Tech. rep., met.no, 2009. 231, 238

15 Hock, R.: A distributed temperature-index ice-and snowmelt model including potential direct solar radiation, J. Glaciol., 45, 101–111, 1999. 212

Hock, R. and Holmgren, B.: A distributed surface energy-balance model for complex topography and its application to Storglaciaren, Sweden, J. Glaciol., 51, 25–36, 2005. 213

Hock, R. and Radic, V.: Climate sensitivity of Storglaciaren, Sweden: an intercomparison
20 of mass-balance models using ERA-40 re-analysis and regional climate model data, Ann. Glaciol., 46, 342–348, 2007. 213

Houghton, H.: On the Annual Heat Balance of the Northern Hemisphere, J. Atmos. Sci., 11, 1–9, 1954. 219, 225

IPCC: Climate Change 2001: The Scientific Basis. Contribution of Working Group I to the
25 Third Assessment Report of the Intergovernmental Panel on Climate Change, Cambridge University Press, 2001. 236

Jansson, P., Hock, R., and Schneider, T.: The concept of glacier storage: a review, J. Hydrol., 282, 116–129, 2003. 213

Klok, E. and Oerlemans, J.: Model study of the spatial distribution of the energy and mass
30 balance of Morteratschgletscher, Switzerland, J. Glaciol., 48, 505–518, 2002. 213, 219, 225, 226, 240

Koerner, R.: Some observations on superimposition of ice on the Devon Island ice cap, NWT Canada, Geografiska Annaler, Series A. Phys. Geogr., 52, 57–67, 1970. 213

Kondratyev, K.: Radiation in the Atmosphere, Academic Press, Inc., 1969. 219

Konzelmann, T., van de Wal, R., Greuell, W., Bintanja, R., Henneken, E., and Abe-Ouchi, A.: Parameterization of global and longwave incoming radiation for the Greenland ice sheet, Glob. Planet. Change, 9, 143–164, 1994. 220, 225

Korona, J., Berthier, E., Bernard, M., Rémy, F., and Thouvenot, E.: SPIRIT. SPOT 5 stereoscopic survey of Polar Ice: Reference Images and Topographies during the fourth International Polar Year (2007–2009), ISPRS J. Photogr. Remote Sens., 64, 204–212, 2009. 215

Kuipers Munneke, P., Reijmer, C., van den Broeke, M., Stammes, P., König-Langlo, G., and Knap, W.: Analysis of clear-sky Antarctic snow albedo using observations and radiative transfer modeling, J. Geophys. Res, 113, D17118 doi:10.1029/2007JD009653, 2008. 225

Ligtenberg, S. R. M., Helsen, M. M., and van den Broeke, M. R.: An improved semi-empirical model for the densification of Antarctic firn, The Cryosphere, 5, 809–819, doi:10.5194/tc-5-809-2011, 2011. 221, 222

McDonald, J.: Direct Absorption of Solar Radiation by Atmospheric Water Vapor, J. Atmos. Sci., 17, 319–328, 1960. 219

Meier, M.: Glaciers and climate, The Quaternary of the United States, 795–804, 1965. 212

Obleitner, F. and Lehning, M.: Measurement and simulation of snow and superimposed ice at the Kongsvegen glacier, Svalbard (Spitzbergen), J. Geophys. Res., 109, D04106, doi:10.1029/2003JD003945, 2004. 213

Oerlemans, J. and Grisogono, B.: Glacier winds and parameterisation of the related surface heat fluxes, Tellus A, 54, 440–452, 2002. 217, 220, 227

Oerlemans, J. and Klok, E.: Effect of summer snowfall on glacier mass balance, Ann. Glaciol., 38, 97–100, 2004. 232

Oerlemans, J. and Knap, W.: A 1 year record of global radiation and albedo in the ablation zone of Morteratschgletscher, Switzerland, J. Glaciol., 44, 147 231–238, 1998. 220

Oerlemans, J. and Reichert, B.: Relating glacier mass balance to meteorological data by using a seasonal sensitivity characteristic, J. Glaciol., 46, 1–6, 2000. 237

Oerlemans, J., Anderson, B., Hubbard, A., Huybrechts, P., Jóhannesson, T., Knap, W. H., Schmeits, M., Stroeven, A. P., van de Wal, R. S. W., Wallinga, J., and Zuo, Z.: Modelling the response of glaciers to climate warming, Clim. Dynam., 14, 267–274, 1998. 212

Pälli, A., Kohler, J., Isaksson, E., Moore, J., Pinglot, J., Pohjola, V., and Samuelsson, H.: Spatial and temporal variability of snow accumulation using ground-penetrating radar and ice cores on a Svalbard glacier, J. Glaciol., 48, 417–424, 2002. 216, 227, 228, 242

Melt, runoff and refreezing on Nordenskiöldbreen

W. J. J. van Pelt et al.

Paterson, W.: The physics of glaciers, Pergamon, New York, 1994. 213

Pettersson, R.: Dynamics of the cold surface layer of polythermal Storglaciären, Sweden, PhD diss, Stockholm University. Department of Physical Geography and Quaternary Geology, Stockholm University Dissertation Series, 2004. 233

5 Pfeffer, W., Meier, M., and Illangasekare, T.: Retention of Greenland runoff by refreezing: implications for projected future sea level change, J. Geophys. Res, 96, 117–22, 1991. 213

Pohjola, V., Martma, T., Meijer, H., Moore, J., Isaksson, E., Vaikmae, R., and van de Wal, R.: Reconstruction of three centuries of annual accumulation rates based on the record of stable isotopes of water from Lomonosovfonna, Svalbard, Ann. Glaciol., 35, 57–62, 2002a. 239

10 Pohjola, V., Moore, J., Isaksson, E., Jauhiainen, T., van de Wal, R., Martma, T., Meijer, H., and Vaikmäe, R.: Effect of periodic melting on geochemical and isotopic signals in an ice core from Lomonosovfonna, Svalbard, J. Geophys. Res, 107, 4036, doi:10.1029/2000JD000149, 2002b. 218, 228, 253

Raper, S. and Braithwaite, R.: Low sea level rise projections from mountain glaciers and ice-caps under global warming, Nature, 439, 311–313, 2006. 212

15 Reijmer, C. and Hock, R.: Internal accumulation on Storglaciaren, Sweden, in a multi-layer snow model coupled to a distributed energy-and mass-balance model, J. Glaciol., 54, 61–72, 2008. 213, 220, 223

Schneider, T. and Jansson, P.: Internal accumulation in firn and its significance for the mass balance of Storglaciaren, Sweden, J. Glaciol., 50, 25–34, 2004. 213, 222

20 Schoof, C.: Ice-sheet acceleration driven by melt supply variability, Nature, 468, 803–806, 2010. 213, 243

Schytt, V.: Re-freezing of the melt-water on the surface of glacier ice, Geograf. Ann., 31, 222–227, 1949. 213

25 Sturm, M., Holmgren, J., König, M., and Morris, K.: The thermal conductivity of seasonal snow, J. Glaciol., 43, 26–41, 1997. 221

Trabant, D. and Mayo, L.: Estimation and effects of internal accumulation on five glaciers in Alaska, Ann. Glaciol., 6, 113–117, 1985. 213

Van de Wal, R., Mulvaney, R., Isaksson, E., Moore, J., Pinglot, J., Pohjola, V., and Thomassen,

30 M.: Reconstruction of the historical temperature trend from measurements in a medium-length borehole on the Lomonosovfonna plateau, Svalbard, Ann. Glaciol., 35, 371–378, 2002. 218, 228, 253

Van de Wal, R., Boot, W., van den Broeke, M., Smeets, C., Reijmer, C., Donker, J., and Oerle-

mans, J.: Large and rapid melt-induced velocity changes in the ablation zone of the Greenland Ice Sheet, Science, 321, 111–113, doi:10.1126/science.1158540, 2008. 213, 243

Van den Broeke, M., van As, D., Reijmer, C., and van de Wal, R.: Assessing and improving the quality of unattended radiation observations in Antarctica, J. Atmos. Ocean. Technol., 21, 1417–1431, 2004. 225

Van den Broeke, M., Reijmer, C., van As, D., and Boot, W.: Daily cycle of the surface energy balance in Antarctica and the influence of clouds, Int. J. Climatol., 26, 1587–1605, 2006. 225

Wadham, J. and Nuttall, A.: Multiphase formation of superimposed ice during a mass-balance year at a maritime high-Arctic glacier, J. Glaciol., 48, 545–551, 2002. 213

Wright, A., Wadham, J., Siegert, M., Luckman, A., and Kohler, J.: Modelling the impact of superimposed ice on the mass balance of an Arctic glacier under scenarios of future climate change, Ann. Glaciol., 42, 277–283, 2005. 213

Yen, Y.: Review of thermal properties of snow, ice and sea ice, Tech. rep., DTIC Document, 1981. 221

Zuo, Z. and Oerlemans, J.: Modelling albedo and specific balance of the Greenland ice sheet: calculations for the Søndre Strømfjord transect, J. Glaciol., 42, 305–317, 1996. 223

Zwally, H., Abdalati, W., Herring, T., Larson, K., Saba, J., and Steffen, K.: Surface melt-induced acceleration of Greenland ice-sheet flow, Science, 297, 218–222, doi:10.1126/science.1072708, 2002. 213, 243

Melt, runoff and refreezing on Nordenskiöldbreen

W. J. J. van Pelt et al.

Title Page

Abstract | Introduction

Conclusions | References

Tables | Figures

◄ | ►►

◄ | ►

Back | Close

Full Screen / Esc

Printer-friendly Version

Interactive Discussion

Table 1. Overview of the mass balance sensitivity (δMB), refreezing sensitivity (δRE) and runoff sensitivity (δRU) to perturbations of a selection of model parameters. Sensitivities are given in mm w.e. a^{-1}.

Parameter	Value	Perturbation	δMB	δRE	δRU
C_b	0.0028	+0.0010	−6.1	−7.0	−2.8
		−0.0010	0.3	7.5	−3.1
γ_p (m km^{-1})	0.370	+0.050	67.2	5.1	33.6
		−0.050	−74.4	−5.9	−40.7
a_{max} (m w.e.)	0.54	+0.10	4.2	0.2	−0.1
		−0.10	−41.7	7.3	−1.0
ϵ_{cl}	0.990	+0.01	−87.5	−0.6	−85.7
		−0.01	81.0	−0.5	79.1
b	0.447	+0.010	−25.6	−3.0	−24.6
		−0.010	24.6	3.0	23.6
k	0.97	+0.01	−53.3	−0.7	−52.8
		−0.01	50.2	0.5	49.7
ρ_{fs} (kg m^{-3})	300	+25	−7.8	2.5	−7.7
		−25	2.3	−4.9	2.2
α_{ice}	0.32	+0.03	24.1	0.1	24.1
		−0.03	−24.3	−0.1	−24.2
α_{fs}	0.87	+0.03	118.0	−0.8	116.1
		−0.03	−138.9	−2.1	−137.2
C_{ro}	1	×2	−0.7	0.8	−0.7
		/2	0.6	−0.6	0.5
$T_{s/r}$ (K)	274.6	+0.5	32.3	1.6	32.2
		−0.5	−40.7	−1.3	−40.6
P_{fs} (mm h^{-1})	0.04	+0.01	−52.3	−1.5	−51.9
		−0.01	40.9	1.1	40.7

Table 2. Overview of the mass balance sensitivity (δMB), refreezing sensitivity (δRE) and ELA sensitivity (δELA) to changes in air temperature T and precipitation P. Sensitivities are given in m w.e. a^{-1} for the mass balance and refreezing sensitivity and m a.s.l. for the ELA sensitivity. The non-seasonal δELA in the run with $T + 4$ K could not be resolved since the ELA in this scenario is above the highest point on the grid. Mass balance, refreezing and ELA values in the unperturbed climate run are −0.448 m w.e. a^{-1}, 0.259 m w.e. a^{-1} and 724 m a.s.l., respectively.

Run	No seasonality			With seasonality		
	δMB	δRE	δELA	δMB	δRE	δELA
$T - 4$ K	+0.78	−0.046	−402	+0.51	+0.012	−150
$T - 3$ K	+0.68	−0.014	−285	+0.41	+0.013	−120
$T - 2$ K	+0.52	+0.008	−169	+0.30	+0.011	−86
$T - 1$ K	+0.29	+0.013	−90	+0.16	+0.006	−44
$T + 1$ K	−0.36	−0.017	+103	−0.21	−0.005	+34
$T + 2$ K	−0.79	−0.034	+225	−0.46	−0.009	+102
$T + 3$ K	−1.27	−0.047	+366	−0.77	−0.010	+175
$T + 4$ K	−1.79	−0.056		−1.18	−0.015	+236
$P - 40\%$	−0.55	−0.051	+175	−0.56	−0.053	+183
$P - 30\%$	−0.38	−0.033	+134	−0.39	−0.035	+132
$P - 20\%$	−0.27	−0.029	+110	−0.24	−0.022	+86
$P - 10\%$	−0.11	−0.009	+37	−0.11	−0.010	+38
$P + 10\%$	+0.10	+0.008	−19	0.10	+0.009	−17
$P + 20\%$	+0.19	+0.015	−48	0.19	+0.016	−45
$P + 30\%$	+0.27	+0.022	−75	0.27	+0.024	−73
$P + 40\%$	+0.34	+0.028	−100	0.34	+0.030	−94
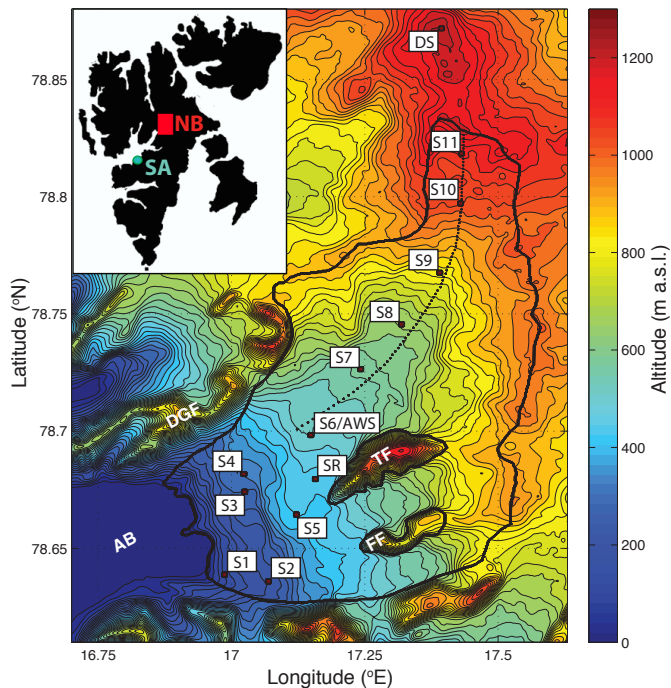
Fig. 1. Contour plot of the surface topography. The glacier outline is indicated by the thick black line. Dark red squares mark the position of the stake sites (S1–11), the Automatic Weather Station (AWS), the Sonic Ranger (SR) and the ice core drilling site (DS). The location of De Geerfjellet, Terrierfjellet, Ferrierfjellet and the Adolfbukta fjord are denoted by DGF, TF, FF and AB respectively. The dashed black line indicates the main flowline and cross-sectional subsurface profiles along this line are shown and discussed in Sect. 5.2. In the inset contour map of Svalbard, the location of Nordenskiöldbreen (NB) and Svalbard Airport (SA) is indicated.
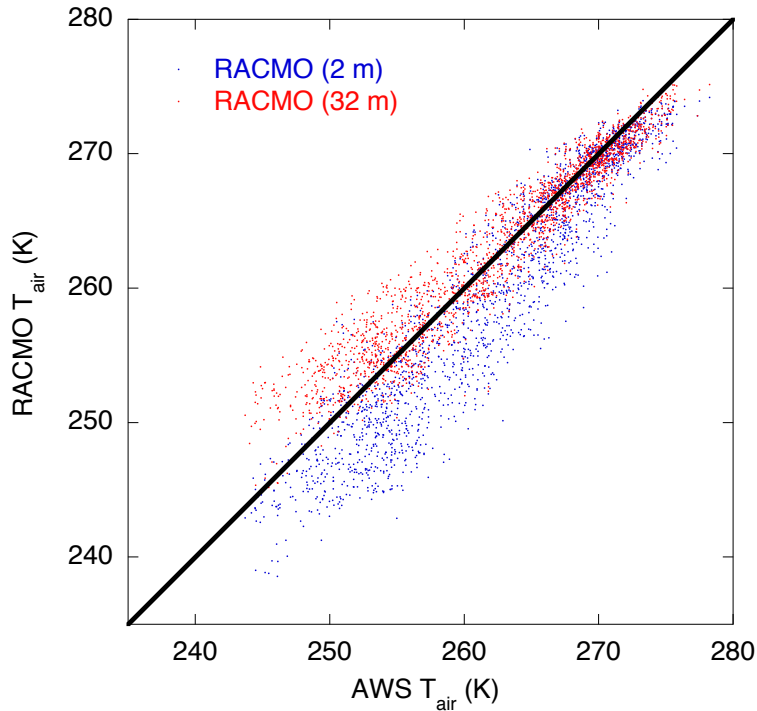
Fig. 2. Scatterplot of 3-hourly RACMO air temperatures at heights of 2 m (blue) and 32 m (red) versus observed air temperatures at ±4 m above the surface at the AWS site for the period March 2009 to November 2010.

Fig. 3. Initialisation of the subsurface temperature (top panel) and density (bottom panel) at the ice core drill site. Observed vertical temperatures are taken from Van de Wal et al. (2002), whereas observed densities are adopted from Pohjola et al. (2002b).
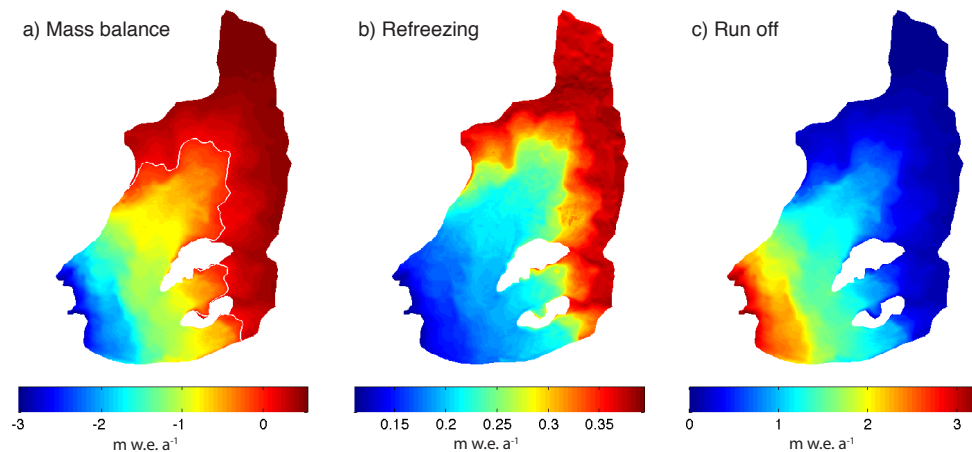
Fig. 4. Contour plots of the annual mean mass balance **(a)**, refreezing **(b)** and runoff **(c)**, averaged over the period 1989–2010. The white line in **(a)** marks the position of the equilibrium line.
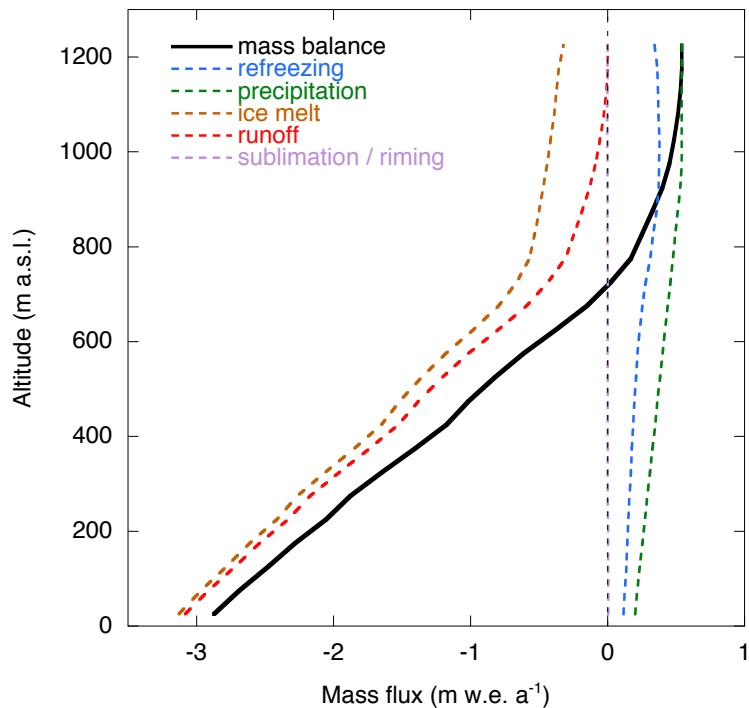
Fig. 5. Height profiles of the mass balance, refreezing, precipitation, ice melt, runoff and the mass flux by sublimation and riming. Data are divided into 25-m bins and averaged over the simulation period 1989–2010.
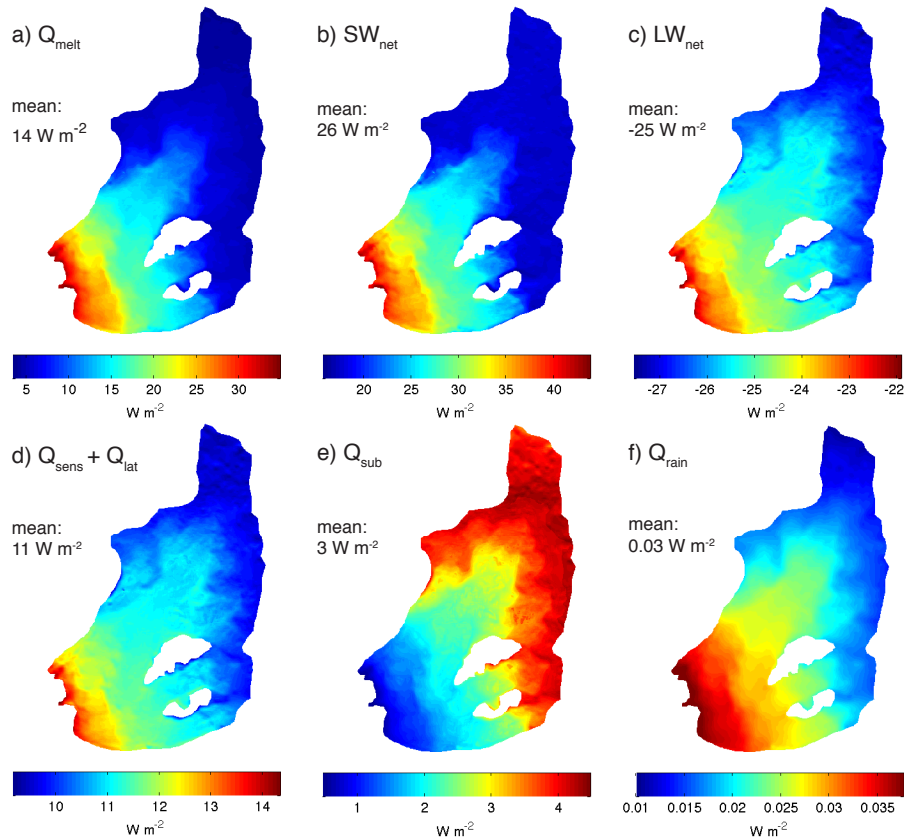
Fig. 6. Contour plots of the melt energy **(a)**, net shortwave radiation **(b)**, net longwave radiation **(c)**, turbulent heat transport **(d)**, the subsurface heat flux **(e)** and the heat supplied by rain **(f)**, averaged over the period 1989–2010.

Title Page

Abstract | Introduction

Conclusions | References

Tables | Figures

⏮ | ⏭

◀ | ▶

Back | Close

Full Screen / Esc

Printer-friendly Version

Interactive Discussion
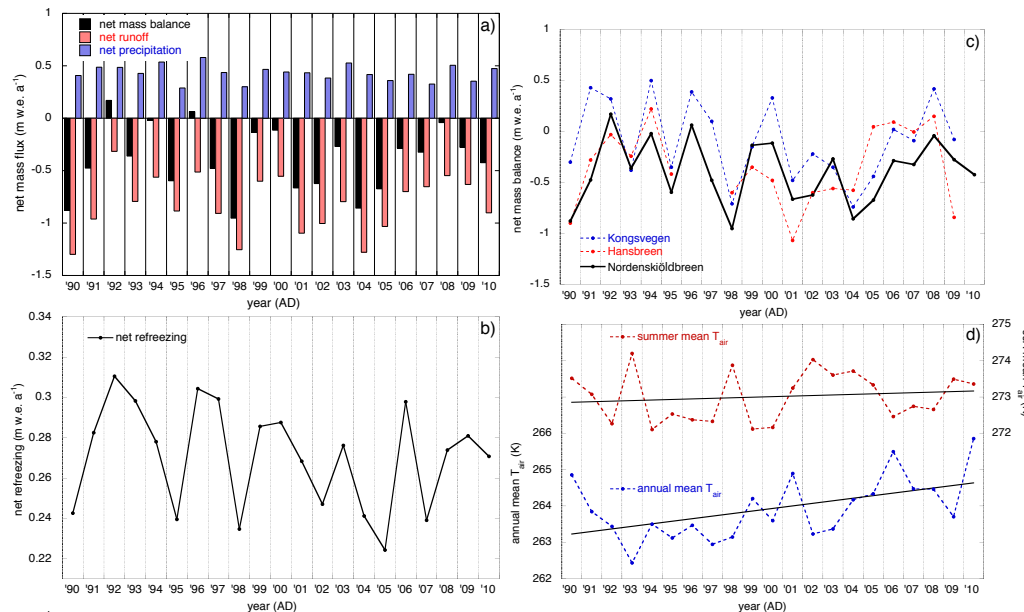
Fig. 7. Time-series over the period 1989–2010 of: **(a)** the net mass balance, precipitation and runoff; **(b)** net annual refreezing; **(c)** the net mass balance for Nordenskiöldbreen (central Svalbard), Kongsvegen (western Svalbard) and Hansbreen (southern Svalbard); and **(d)** spatially averaged annual and summer (JJA) mean air temperatures. The years on the x-axes in this figure represent mass balance years starting at the 1st of October of the preceding year. The black lines in **(d)** mark the linear trend in the annual and summer mean air temperature.
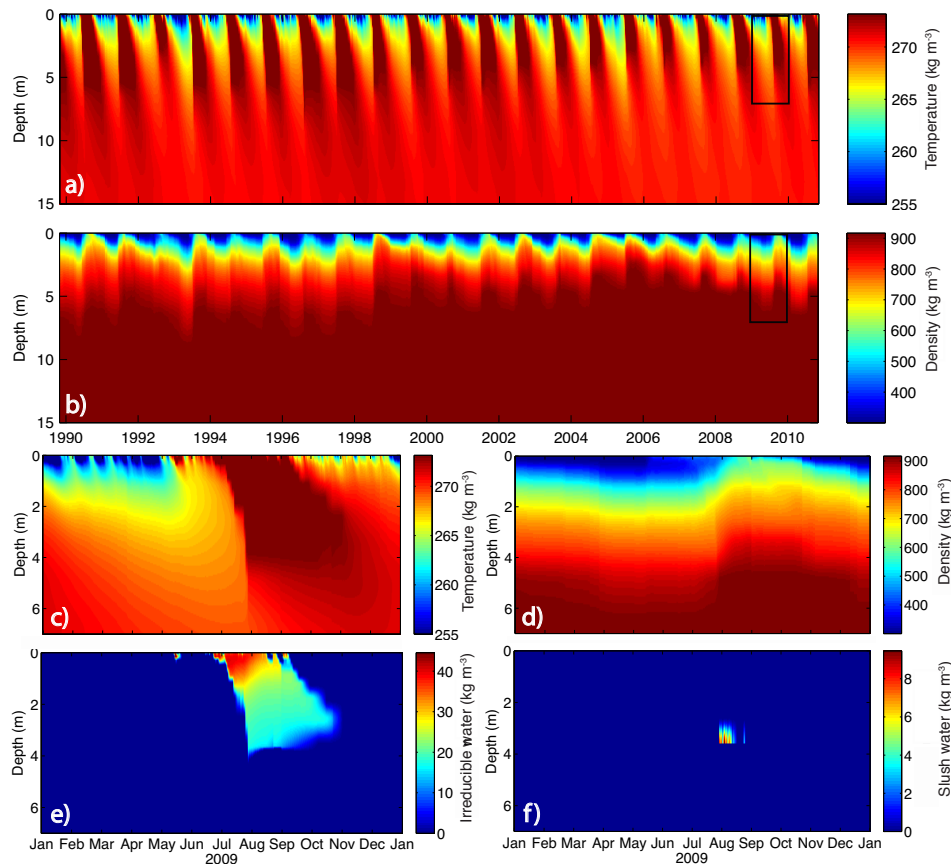
Fig. 8. The upper two panels show time-series of the simulated subsurface temperatures **(a)** and densities **(b)** at stake site S9 over the period 1989–2010. The lower four panels focus on the temperature **(c)**, density **(d)**, irreducible water **(e)** and slush water content **(f)** evolution in 2009 over the time and depth range marked by the black box in the upper two panels.

Title Page

Abstract | Introduction

Conclusions | References

Tables | Figures

◄◄ | ►►

◄ | ►

Back | Close

Full Screen / Esc

Printer-friendly Version

Interactive Discussion
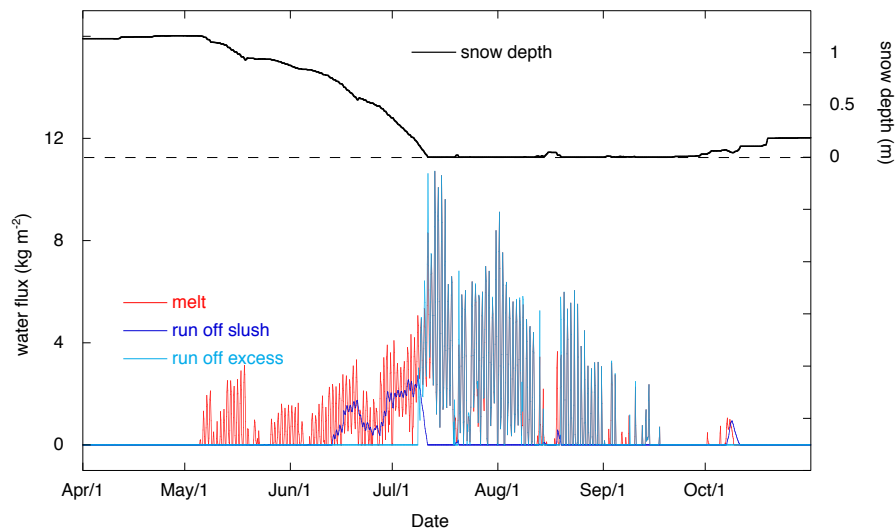
Fig. 9. Runoff time-series of the snow depth, melt and runoff at S6 in the ablation zone for the year 2010.

Printer-friendly Version

Interactive Discussion
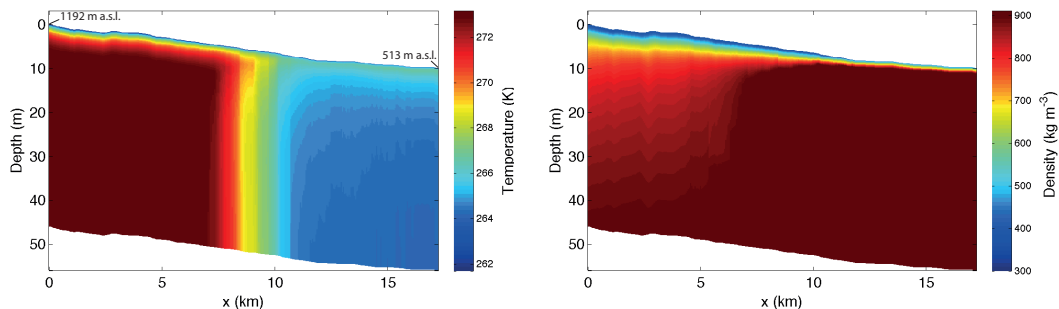
Fig. 10. Cross-sectional vertical profiles of the subsurface temperature (left panel) and density (right panel) along the line marked in Fig. 1. A vertical shift of the profiles is applied to show altitudinal differences along the cross-section.
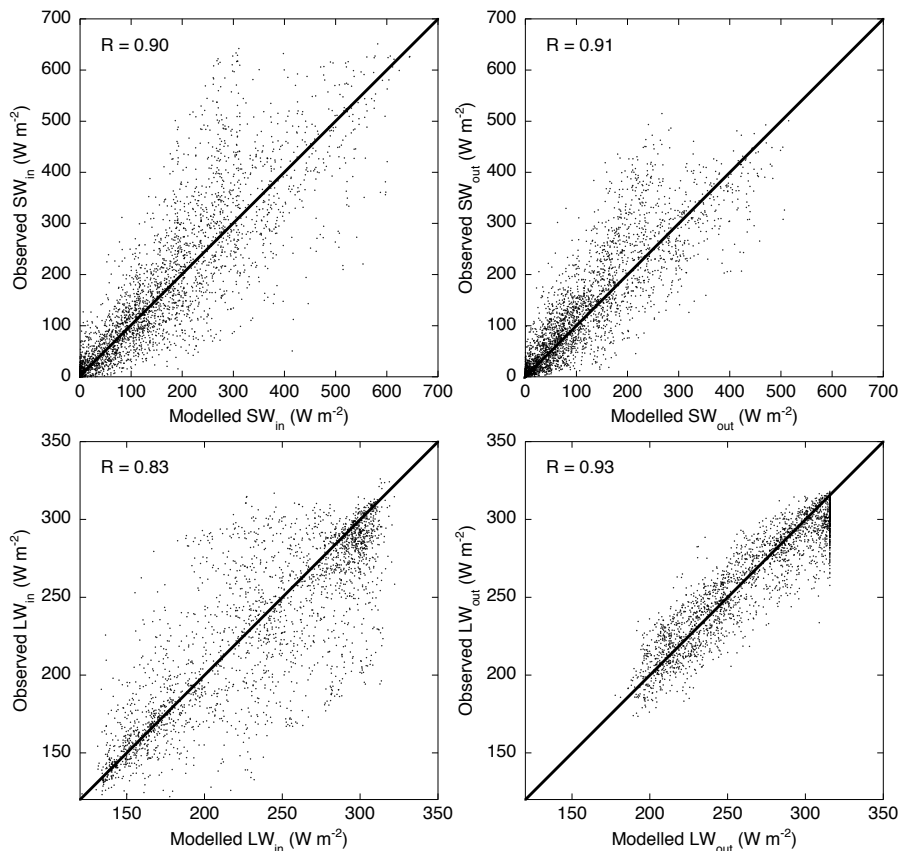
Fig. 11. Scatter plots showing observed (3-hourly) vs. modelled incoming solar radiation (upper left panel), reflected solar radiation (upper right panel), incoming longwave radiation (lower left panel) and outgoing longwave radiation (lower right panel).

Printer-friendly Version

Interactive Discussion
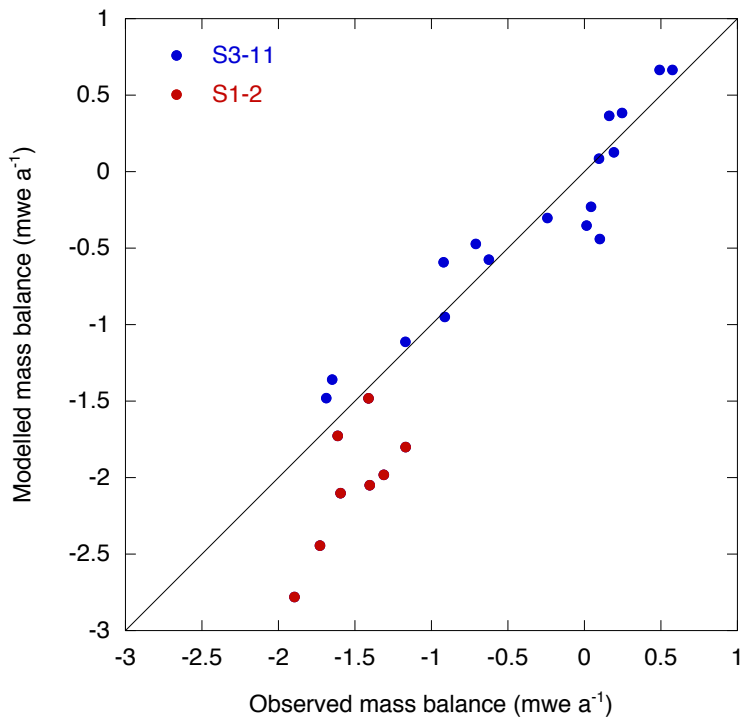
Fig. 12. Scatter plot of simulated mass balance values versus mass balance estimates derived from stake height observations over the period 2006–2010 at sites S1–11.
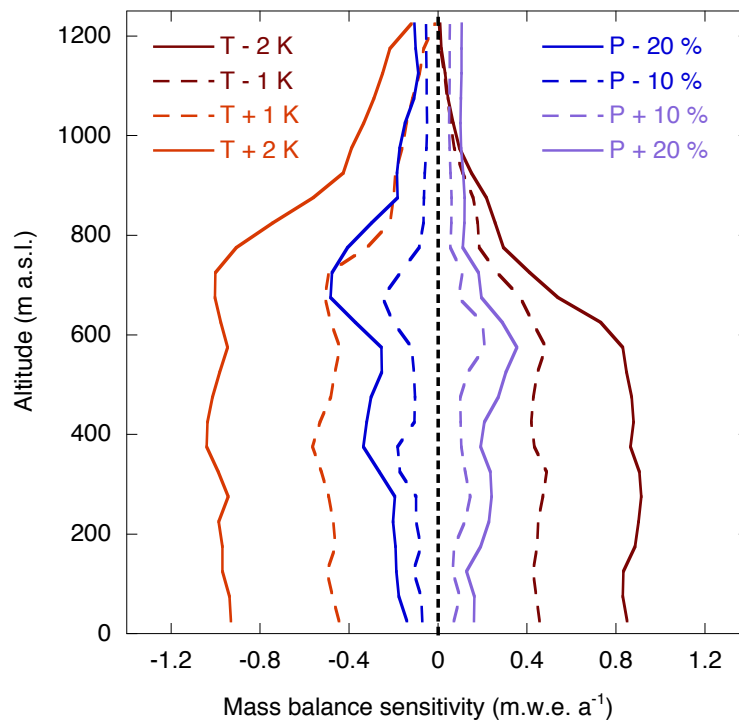
Fig. 13. Height profiles of the mass balance sensitivity to seasonally invariant changes in air temperature T and precipitation P.

Full Screen / Esc

Printer-friendly Version

Interactive Discussion
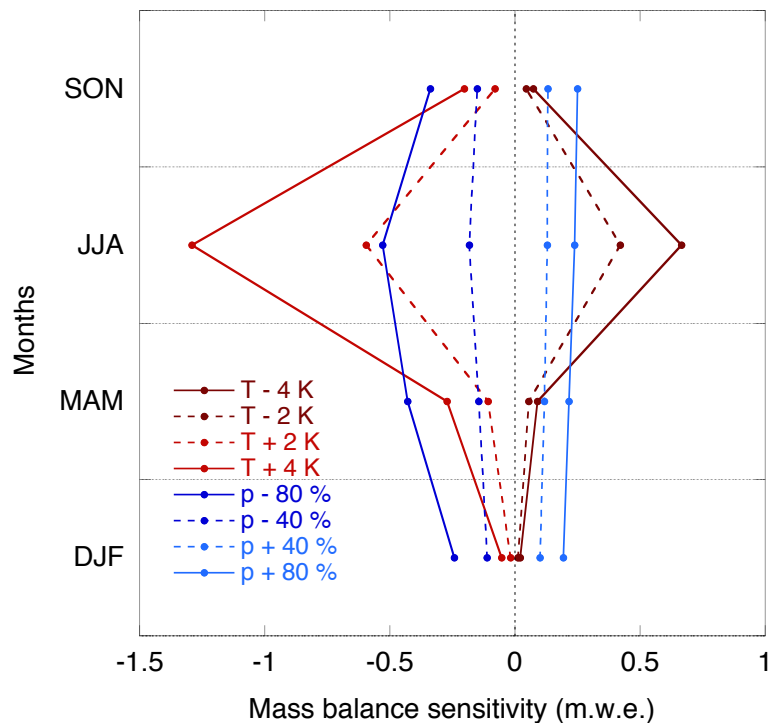
Fig. 14. Annual mass balance sensitivity to seasonally perturbed temperatures (red) and precipitation (blue) over the period 2000–2010.
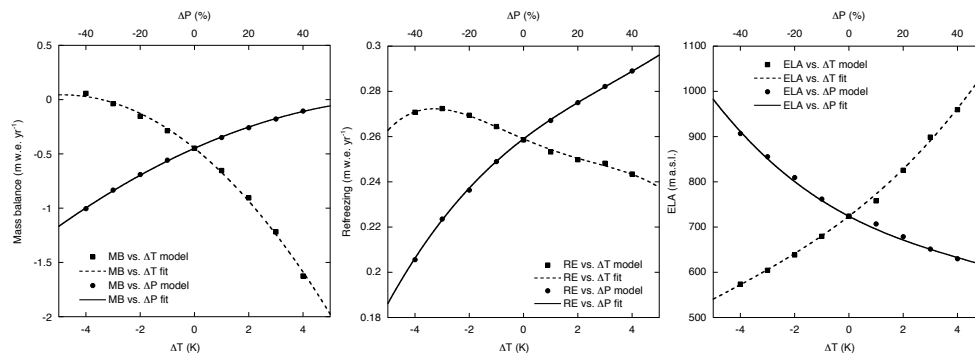
Fig. 15. The simulated net mass balance (left), refreezing (middle) and ELA (right) after seasonally dependent annual perturbations in air temperature and precipitation. Polynomial curves are fitted through the data and used to express the mass balance and ELA as a function of changes in precipitation and temperature.
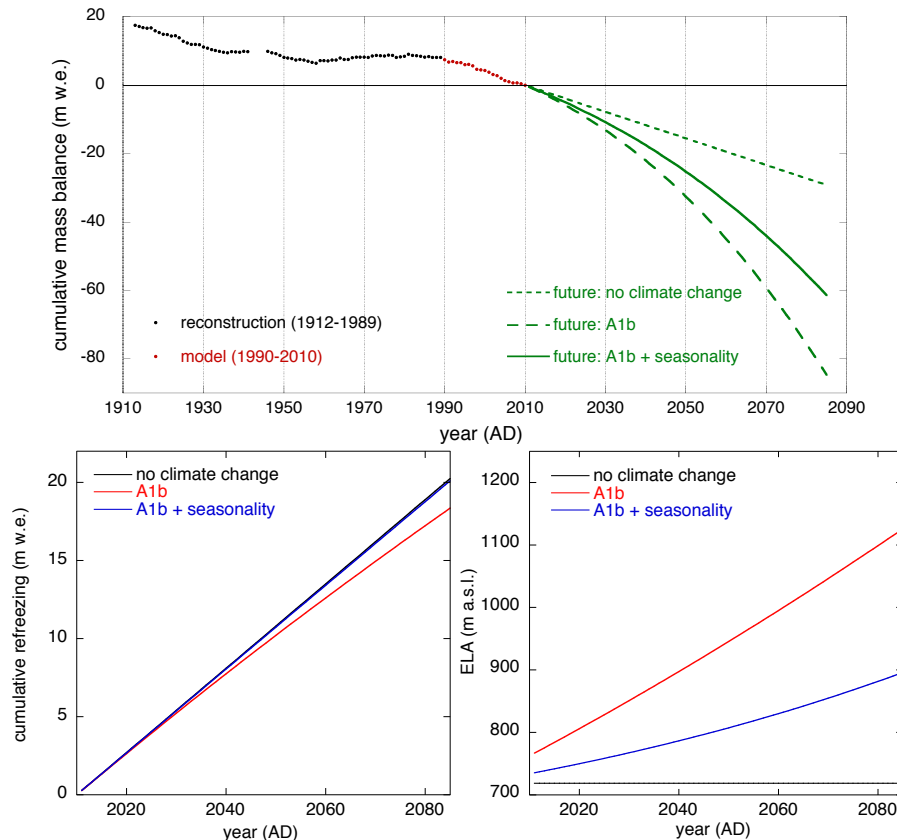
Fig. 16. Time-series of the reconstructed (1912–1989), simulated (1990–2010) and projected (2011–2085) cumulative mass balance (top panel). The lower panels show the projected cumulative refreezing (left) and ELA (right) over the period 2011–2085. The net mass balance for 1942–1944 is set to zero, since we lack reconstructed estimates of precipitation during this period.

Title Page

Abstract | Introduction

Conclusions | References

Tables | Figures

◄◄ | ►►

◄ | ►

Back | Close

Full Screen / Esc

Printer-friendly Version

Interactive Discussion